NTNU

Norwegian University of
Science and Technology

High Order Numerical Simulation of Viscous Compressible Flow in a Simplified Geometry of the Human Upper Airways

Petra Tisovská

Master of Science in Mechanical Engineering
Submission date: June 2017
Supervisor: Bernhard Müller, EPT

Norwegian University of Science and Technology
Department of Energy and Process Engineering

NTNU – Trondheim
Norwegian University of
Science and Technology

High Order Numerical Simulation of Viscous Compressible Flow in a Simplified Geometry of the Human Upper Airways

Petra Tisovská

June 2017

MASTER THESIS

Department of Energy and Process Engineering

Norwegian University of Science and Technology

Supervisor: Bernhard Müller, EPT

NTNU

Norwegian University
of Science and Technology

Department of Energy
and Process Engineering

EPT-M-2017-88

MASTER THESIS

for

Student Petra Tisovská

Spring 2017

High Order Numerical Simulation of Viscous Compressible Flow in a Simplified Geometry of the Human Upper Airways

Høyre ordens numerisk simulering av viskøs kompressibel strømning i en forenklet geometri av de menneskelige øvre luftveier

Background and objective

Snoring is caused by the soft parts of the upper airways collapsing and preventing the air from flowing freely. In some cases snoring is so severe that medical attention is required. The most severe, obstructive sleep apnea syndrome (OSAS), affects 2-4 % of the population. A variety of treatment options exists, but today there are no available methods for predicting the outcome of the treatment. This master project will be part of a larger project: *Modeling of obstructive sleep apnea by fluid-structure interaction in the upper airways*, which is a collaboration project between NTNU, SINTEF and St.Olavs Hospital and funded by the Research Council of Norway. The objective of the research project is to develop a clinical tool to predict the response of surgeries for Obstructive Sleep Apnea Syndrome (OSAS) patients and to identify the decisive pathophysiological mechanisms for the development of OSAS.

The objective of the master project is to simulate viscous compressible flow in a simplified geometry of the human upper airways using a high order compressible Navier-Stokes solver. A high order two-dimensional (2D) compressible Navier-Stokes code for flow over a plate in a channel is to be extended to three dimensions (3D), to be implemented on a high performance computing (HPC) cluster at NTNU using multi-block structured grids and message passing interface (MPI), and to be verified and validated.

The following tasks are to be considered:

1. to get a basic physical understanding of viscous compressible flow, its mathematical description and its numerical solution by a high order difference method,
2. to extend an existing high order 2D compressible Navier-Stokes code to 3D,
3. to implement the high order 3D compressible Navier-Stokes code on a HPC cluster,
4. to verify the high order 3D compressible Navier-Stokes code,
5. to validate the high order 3D compressible Navier-Stokes code for flow in a simplified geometry of the human upper airways.

Within 14 days of receiving the written text on the master thesis, the candidate shall submit a research plan for his project to the department.

When the thesis is evaluated, emphasis is put on processing of the results, and that they are presented in tabular and/or graphic form in a clear manner, and that they are analyzed carefully.

The thesis should be formulated as a research report with summary both in English and Norwegian, conclusion, literature references, table of contents etc. During the preparation of the text, the candidate should make an effort to produce a well-structured and easily readable report. In order to ease the evaluation of the thesis, it is important that the cross-references are correct. In the making of the report, strong emphasis should be placed on both a thorough discussion of the results and an orderly presentation.

The candidate is requested to initiate and keep close contact with his/her academic supervisor(s) throughout the working period. The candidate must follow the rules and regulations of NTNU as well as passive directions given by the Department of Energy and Process Engineering.

Risk assessment of the candidate's work shall be carried out according to the department's procedures. The risk assessment must be documented and included as part of the final report. Events related to the candidate's work adversely affecting the health, safety or security, must be documented and included as part of the final report. If the documentation on risk assessment represents a large number of pages, the full version is to be submitted electronically to the supervisor and an excerpt is included in the report.

Pursuant to “Regulations concerning the supplementary provisions to the technology study program/Master of Science” at NTNU §20, the Department reserves the permission to utilize all the results and data for teaching and research purposes as well as in future publications.

The final report is to be submitted digitally in DAIM. An executive summary of the thesis including title, student’s name, supervisor's name, year, department name, and NTNU's logo and name, shall be submitted to the department as a separate pdf file. Based on an agreement with the supervisor, the final report and other material and documents may be given to the supervisor in digital format.

☐ Work to be done in lab (Water power lab, Fluids engineering lab, Thermal engineering lab)
☐ Field work

Department of Energy and Process Engineering, 15. January 2017

Bernhard Müller
Academic Supervisor

Abstract

This master's thesis is a part of an interdisciplinary research project dealing with modeling of obstructive sleep apnea syndrome (OSAS). Its main goal is to extend an existing 2D code for compressible flow into the third dimension and verify it. The code solves the compressible Navier-Stokes equations by a high order finite difference method. The message passing interface (MPI) has been used for parallelization. The results are compared with results from the 2D program. Grid refinement studies are made, and 3D structures are observed in a simulation that is run on a grid with high-resolution on the high performance computing cluster Vilje.

Acknowledgments

I would like to thank to supervisor Bernhard Müller for his great help during the work. Without his willingness to answer my questions I would not be able to finalize every part of my work. The same amount of gratitude goes to Ehsan Khalili. My thanks go to my colleague Robert Seidel for his work on the parallel interpretation of this program. I would like to thank doc. Ing. Petr Šidlof, Ph.D. for his suggestions for this thesis. Last but not least, I would like to thank my family for their great support.

Also I would like to thank the whole team of this project, the people from NTNU, SINTEF and St. Olavs Hospital, who are trying to help patients with OSAS. Thank you for creating this research group and for letting me be part of it.

P. T.

Contents

List of Figures

List of Tables

Legend

$(\rho E)_0$ stagnation value of total energy density

Δt time step

κ heat conduction coefficient

λ_i eigenvalues

η transformed coordinate

ξ transformed coordinate

ζ transformed coordinate

$\mathbf{d}$ vector, function of $\mathscr{L}$

$\mathbf{F}'^c$ inviscid perturbation flux vector in x-direction

$\mathbf{F}'^v$ viscous perturbation flux vector in x-direction

$\mathbf{G}'^c$ inviscid perturbation flux vector in y-direction

$\mathbf{G}'^v$ viscous perturbation flux vector in y-direction

$\mathbf{H}'^c$ inviscid perturbation flux vector in z-direction

$\mathbf{H}'^v$ viscous perturbation flux vector in z-direction

$\mathbf{Q}$ summation by parts operator

$\mathbf{R}(\mathbf{U})$ residuals function of conservative variables

$\mathbf{U}'$ vector of conservative perturbation variables

$\mathbf{u}'$ perturbation velocity vector

$\mathscr{L}$ vector containing the wave amplitude variations

μ viscosity

ρ density

ρ_0 stagnation density

τ viscous stress tensor

A amplitude of acoustic wave

c speed of sound

c_p heat capacity at constant pressure

c_v heat capacity at constant volume

E specific total energy

H total enthalpy

J Jacobian determinant of Coordinate transformation

M Mach number

p pressure

Pr Prandtl number

R specific gas constant

Re Reynolds number

T temperature

u velocity component in x-direction

v velocity component in y-direction

w velocity component in z-direction

x Cartesian coordinate

y Cartesian coordinate

z Cartesian coordinate

Acronyms

CFD Computational fluid dynamics

CFL Courant-Friedrichs-Lewy number

LODI Local one-dimensional inviscid relations

NSCBC Navier-Stokes characteristic boundary conditions

MPI Message passing interface

NTNU Norwegian University of Science and Technology

OSA Obstructive sleep apnea

REM Rapid eye movement sleep, phase of sleep when muscles are relaxed

RK Runge-Kutta

SBP Summation by parts

VNN Von Neumann number

Chapter 1

Introduction

This chapter gives an introduction to obstructive sleep apnea, its causes, symptoms and ways of treatment. The main tasks of the research group are introduced and how this master thesis is related to that work.

1.1 Obstructive Sleep Apnea

According to Ho [3] obstructive sleep apnea is characterized by recurrent episodes of obstruction of the upper airway, which make that the patient repeatedly stop breathing during sleep. The obstruction is caused by the collapsing soft palate blocking the airway in the phase of sleep when the muscles are relaxed called rapid eye movement (REM) phase.

Figure 1.1 shows how the soft palate behaves in different stages. The left sketch illustrates normal behavior where air flows freely during sleep. In the middle sketch, the soft palate causes snoring by collapsing and blocking the air from the nose. The right sketch shows the OSA case. The soft palate collapse blocks the air from nose and mouth so the brain has to wake up the patient from REM

phase of sleep to obtain some air. This figure is taken from [1].

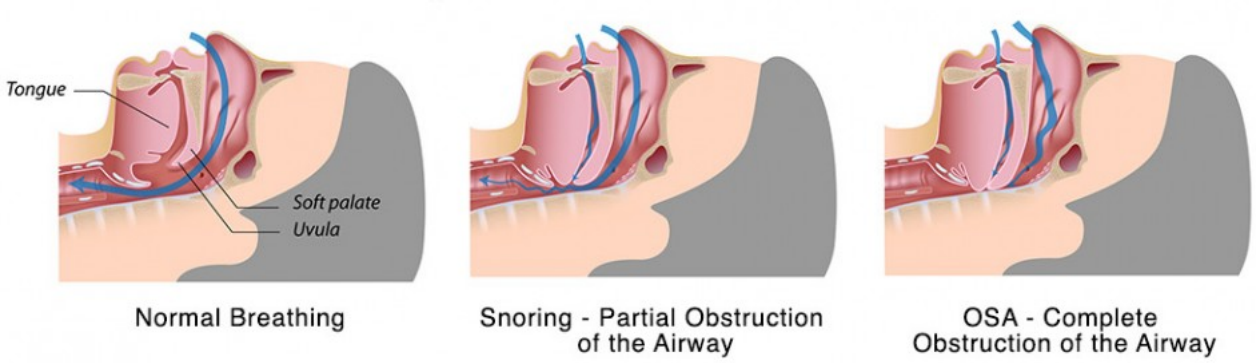

Figure 1.1: Behavior of soft palate in REM sleep [1]

1.1.1 Symptoms

Typically this disease is recognized by family members because it is often connected with snoring. Symptoms are for example day sleepiness, lack of concentration. But OSA can result in prolonged hypoxemia, sleep deprivation, and other complications leading to cardiovascular diseases.
When OSA appears, the brain tries to arouse the body to resume breathing. But it leads to bad quality of sleep.

1.1.2 Treatment

There are two basic ways how to treat this disease, which are mentioned in the Journal of Clinical Sleep Medicine [4]. The methods are behavioral and surgical. The first one is to educate the patient. He or she should lose weight, stop smoking, avoid alcohol and sleeping pills before night, try to change the sleep position. For example reducing neck fat leads to reducing the number of apnea episodes. The second one is surgery. There are lots of ways how to proceed with

operations. Common ones are nasal, oral and hypo pharyngeal procedures [4].

1.1.3 Computational fluid dynamics study of nasal airways

According to [5] physical models reconstructed from Computed tomography (CT) and Magnetic resonance imaging (MRI) images are often impractical and inaccurate. Computational fluid dynamics (CFD) attempt to generate three-dimensional nasal models from various CT scans. Commercial tools are often used for these purposes.

Interesting results were published by [6], where the steady-state simulation was validated by rhinoresistometric data and resin models. Other steady laminar and turbulent simulations were validated by Particle image velocimetry (PIV) investigations of a silicon model by [7]. Hoerschler and Schröder [8] compare steady and unsteady flow in a nose-like model.

1.2 High order finite difference method for the compressible Navier-Stokes equations

High order methods have become more and more popular in CFD. They are used to obtain highly accurate simulations for simple geometries. Such finite difference methods for the compressible Navier-Stokes equations are presented by [9]. High order accurate finite difference summation by parts (SBP) operators are used for discretizing the equations. High efficiency of a 5^{th} order scheme was obtained with $Re = 100$, and robustness was demonstrated. The similar study was made by [10] with different boundary conditions (far-field boundary

conditions) and Reynolds number equal to 500.
Various tests were reviewed for high order methods on unstructured grids [11]. More information about high order methods and their importance for CFD simulations can be found in the review [12].

1.3 Master Project and its Part in Research Group

The main goal of the research project "Modeling of obstructive sleep apnea" currently performed by NTNU, SINTEF and St. Olavs Hospital [13] is to find out if nasal surgery will be successful. Up to now, there is no way how to find this out before the surgery is done. The success rate is less than 50 %. In 10 % of the cases, the post-operative state is worse than before the operation.

The work is divided into 4 work packages:

- WP1 Clinical Research
- WP2 Soft Tissue Modeling
- WP3 Mathematical Modeling of Fluid-Structure Interaction
- WP4 CFD Modeling for Prediction of Success of OSAS Surgery

This master's thesis is part of WP3 Mathematical Modeling of Fluid-Structure Interaction. Its main objectives are listed below:

- to extend an existing high order 2D Navier-Stokes code to 3D
- to verify and validate the high order 3D compressible Navier-Stokes code for flow in a simplified geometry of the human upper airways.

1.4 Structure of the Report

The rest of the report is organized as follows: Chapter 2 gives an introduction to viscous compressible flow, the perturbation form of the compressible Navier-Stokes equations, coordinate transformation and boundary conditions.
Then numerical methods used in the program are introduced in chapter 3. Also numerical boundary conditions are described there, such as non-reflecting and periodic boundary conditions.
The chapter 4 describes results for various test cases. This chapter deals with verification and validation. Conclusions and outlook are given in chapter 5.
Appendix A gives a brief manual how to upload the code into the high-performance computational cluster Vilje.

Chapter 2

Compressible fluid flow

This chapter contains the description of the equations the equations modeling the compressible fluid flow and their transformation into different coordinate systems. The 3D Navier-Stokes equations are used in dimensionless perturbation form. This form was chosen to minimize computational errors when discretizing the Navier-Stokes equations at low Mach numbers.

2.1 Nondimensional 3D Navier-Stokes equations in perturbation form

According to [14] the conservative form of the 3D Navier-Stokes equation in perturbation formulation is written as

$$\mathbf{U}'_t + \mathbf{F}'^c_x + \mathbf{G}'^c_y + \mathbf{H}'^c_z = \mathbf{F}'^v_x + \mathbf{G}'^v_y + \mathbf{H}'^v_z, \tag{2.1}$$

where $\mathbf{U}'$ is vector of conservative perturbation variables and defined by

$$\mathbf{U}' = \mathbf{U} - \mathbf{U}_0 = \begin{pmatrix} \rho \\ \rho u \\ \rho v \\ \rho w \\ \rho E \end{pmatrix} - \begin{pmatrix} \rho_0 \\ 0 \\ 0 \\ 0 \\ (\rho E)_0 \end{pmatrix}, \tag{2.2}$$

where ρ is the density, u, v and w are the velocity components in x-, y-, and z-directions and E is the specific total energy. The subscripts in 2.1 denote derivatives, i. e., $\mathbf{U}'_t = \frac{\partial \mathbf{U}'}{\partial t}$, $\mathbf{F}'^c_x = \frac{\partial \mathbf{F}'^c}{\partial x}$, etc.

The inviscid perturbation flux vectors $\mathbf{F}'^c$, $\mathbf{G}'^c$ and $\mathbf{H}'^c$ and viscous perturbation flux vectors $\mathbf{F}'^v$, $\mathbf{G}'^v$ and $\mathbf{H}'^v$ are defined by

$$\mathbf{F}'^c = \begin{pmatrix} (\rho u)' \\ (\rho u)' u' + p' \\ (\rho v)' u' \\ (\rho w)' u' \\ ((\rho H)_0 + (\rho H)') u' \end{pmatrix}, \tag{2.3}$$

$$\mathbf{G}'^c = \begin{pmatrix} (\rho v)' \\ (\rho u)' v' \\ (\rho v)' v' + p' \\ (\rho w)' v' \\ ((\rho H)_0 + (\rho H)') v' \end{pmatrix}, \tag{2.4}$$

$$\mathbf{H}'^{c} = \begin{pmatrix} (\rho w)' \\ (\rho u)' w' \\ (\rho v)' w' \\ (\rho w)' w' + p' \\ ((\rho H)_0 + (\rho H)') w' \end{pmatrix}, \tag{2.5}$$

$$\mathbf{F}'^{v} = \begin{pmatrix} 0 \\ \tau'_{xx} \\ \tau'_{xy} \\ \tau'_{xz} \\ u'\tau'_{xx} + v'\tau'_{xy} + w'\tau'_{xz} + \kappa T'_x \end{pmatrix}, \tag{2.6}$$

$$\mathbf{G}'^{v} = \begin{pmatrix} 0 \\ \tau'_{yx} \\ \tau'_{yy} \\ \tau'_{yz} \\ u'\tau'_{yx} + v'\tau'_{yy} + w'\tau'_{yz} + \kappa T'_y \end{pmatrix}, \tag{2.7}$$

$$\mathbf{H}'^{v} = \begin{pmatrix} 0 \\ \tau'_{zx} \\ \tau'_{zy} \\ \tau'_{zz} \\ u'\tau'_{zx} + v'\tau'_{zy} + w'\tau'_{zz} + \kappa T'_z \end{pmatrix}, \tag{2.8}$$

where p is pressure, T is temperature, H is total enthalpy, τ_{ij} is the viscous stress tensors component and κ is the heat conduction coefficient calculated from the constant Prandtl number $Pr = 0.72$. The prime denotes the perturbation vari-

able with respect to stagnation condition.

2.1.1 Nondimensional quantities

The symbol $_0$ is used for stagnation variables. They are stagnation density ρ_0, stagnation speed of sound c_0 and stagnation pressure p_0

$$p_0 = \frac{\rho_0 c_0^2}{\gamma}, \tag{2.9}$$

where γ is the ratio of specific heats given by

$$\gamma = \frac{c_p}{c_v}, \tag{2.10}$$

which is $\gamma = 1.4$ for air. c_p is the specific heat at constant pressure and c_v is the specific heat at constant volume.

The nondimensional quantities are defined as follows

$$x^\star = \frac{x}{L} \tag{2.11}$$

$$z^\star = \frac{z}{L} \tag{2.12}$$

$$\rho^\star = \frac{\rho}{\rho_0} \tag{2.13}$$

$$E^\star = \frac{E}{c_0^2} \tag{2.14}$$

$$(\rho E)^\star = \frac{\rho E}{\rho_0 c_0^2} \tag{2.15}$$

$$v^\star = \frac{v}{c_0} \tag{2.16}$$

$$y^\star = \frac{y}{L} \tag{2.17}$$

$$t^\star = \frac{t \cdot c_0}{L} \tag{2.18}$$

$$T^\star = \frac{T}{T_0} \tag{2.19}$$

$$p^\star = \frac{p}{\gamma p_0} \tag{2.20}$$

$$u^\star = \frac{u}{c_0} \tag{2.21}$$

$$w^\star = \frac{w}{c_0} \tag{2.22}$$

$$Re_0 = \frac{\rho_0 c_0 L}{\mu_0} \tag{2.23}$$

$$Pr_0 = \frac{c_p \mu_0 L}{\kappa_0} \tag{2.24}$$

L stands for a characteristics length. Reynolds number Re_0 is defined in terms of the stagnation speed of sound c_0.

A special choice is made for the nondimensional viscosity $\mu^\star$ and the nondimensional heat conduction coefficient $\kappa^\star$:

$$\mu^\star = \frac{1}{Re_0}\frac{\mu}{\mu_0}, \tag{2.25}$$

$$\kappa^\star = \frac{1}{(\gamma-1)Pr_0 Re_0}\frac{\kappa}{\kappa_0}. \tag{2.26}$$

With this choice, the nondimensional and dimensional forms of the compressible Navier-Stokes equations coincide.

2.1.2 Definition of perturbation variables

The superscript * is skipped below. Dimensionless perturbation variables are defined as follows

density ρ' is:

$$\rho' = \rho - 1. \tag{2.27}$$

The dimensionless perturbation momentum density components $(\rho u)'$, $(\rho v)'$, $(\rho w)'$ are

$$(\rho u)' = (\rho u) \tag{2.28}$$

$$(\rho v)' = (\rho v) \tag{2.29}$$

$$(\rho w)' = (\rho w). \tag{2.30}$$

The dimensionless total energy and total enthalpy density are

$$(\rho E)' = \rho E - (\rho E)_0, \tag{2.31}$$

$$(\rho H)' = (\rho E)' + p' \tag{2.32}$$

where $(\rho E)_0 = \frac{1}{\gamma(\gamma-1)}$ is dimensionless stagnation value of the total energy density. For the viscous stress tensor components dimensionless perturbation velocity vector $\mathbf{u}'$ is needed, which is computed as

$$\mathbf{u}' = \frac{(\rho \mathbf{u})'}{1+\rho'}, \tag{2.33}$$

so viscous stress is:

$$\tau' = \mu(\nabla \mathbf{u}' + (\nabla \mathbf{u}')^T) - \frac{2}{3}\mu(\nabla \cdot \mathbf{u}')\mathbf{I}, \tag{2.34}$$

where $\mathbf{I}$ is identity matrix and μ is the dimensionless viscosity determined from the Sutherland law

$$\mu = \frac{1}{Re} T^{1.5} \frac{1+S_c}{T+S_c} \tag{2.35}$$

and $S_c = \frac{110}{301.75}$ is the nondimensional Sutherland constant. For perfect gas dimensionless temperature perturbation T' is obtained as:

$$T' = \frac{\gamma p' - \rho}{1+\rho}. \tag{2.36}$$

The dimensionless pressure perturbation for perfect gas becomes

$$p' = (\gamma - 1)((\rho E)' - \frac{1}{2}((\rho \mathbf{u})' \cdot \mathbf{u}'). \tag{2.37}$$

2.2 Coordinate transformation of the Navier-Stokes equations

To discretize the compressible Navier-Stokes equations by the finite difference method, the physical domain for flow over a soft palate is transformed into a Cartesian computational domain cf. figure 2.1.

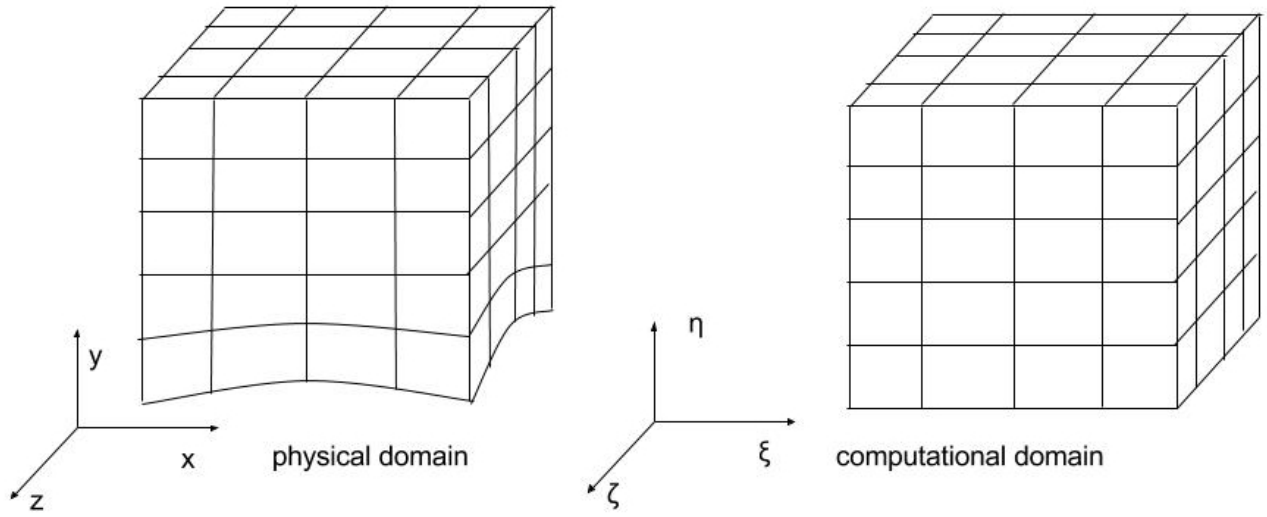

Figure 2.1: Computational and physical domains for over a soft human palate

The transformed coordinates are

$$\xi = (x, y, z), \tag{2.38}$$

$$\eta = (x, y, z), \tag{2.39}$$

$$\zeta = (x, y, z). \tag{2.40}$$

If the physical domain is already Cartesian the ξ represents x-direction, the η represents y-direction and the ζ represents z-direction.

The metric terms of the coordinate transformation are formulated in conservative form to be able to reproduce uniform flow, when the Navier-Stokes equa-

tions and metric terms are discretized by finite difference methods [15].

$$\hat{\xi_x} = (y_\eta z)_\zeta - (y_\zeta z)_\eta, \tag{2.41}$$

$$\hat{\eta_x} = (y_\zeta z)_\xi - (y_\xi z)_\zeta, \tag{2.42}$$

$$\hat{\zeta_x} = (y_\xi z)_\eta - (y_\eta z)_\xi, \tag{2.43}$$

$$\hat{\xi_y} = (z_\eta x)_\zeta - (z_\zeta x)_\eta, \tag{2.44}$$

$$\hat{\eta_y} = (z_\zeta x)_\xi - (z_\xi x)_\zeta, \tag{2.45}$$

$$\hat{\zeta_y} = (z_\xi x)_\eta - (z_\eta x)_\xi, \tag{2.46}$$

$$\hat{\xi_z} = (x_\eta y)_\zeta - (x_\zeta y)_\eta, \tag{2.47}$$

$$\hat{\eta_z} = (x_\zeta y)_\xi - (x_\xi y)_\zeta, \tag{2.48}$$

$$\hat{\zeta_z} = (x_\xi y)_\eta - (x_\eta y)_\xi, \tag{2.49}$$

where $\hat{\xi}$, $\hat{\eta}$ and $\hat{\zeta}$ mean

$$\hat{\xi}_a = \frac{\xi_a}{J}, \tag{2.50}$$

$$\hat{\eta}_a = \frac{\eta_a}{J}, \tag{2.51}$$

$$\hat{\zeta}_a = \frac{\zeta_a}{J}, \tag{2.52}$$

where $a \in \{x, y, z\}$ and $\xi_x = \frac{\partial \xi}{\partial x}$, which is similar for other expressions.

The Jacobian determinant of this transformation is defined as

$$\frac{1}{J} = \begin{vmatrix} x_\xi & y_\xi & z_\xi \\ x_\eta & y_\eta & z_\eta \\ x_\zeta & y_\zeta & z_\zeta \end{vmatrix}. \tag{2.53}$$

The computation of the determinant yields using equations (2.41) – (2.43)

$$\frac{1}{J} = x_\xi \cdot \hat{\xi}_x + x_\eta \cdot \hat{\eta}_x + x_\zeta \cdot \hat{\zeta}_x. \tag{2.54}$$

The 3D Navier-Stokes equations in dimensionless perturbation form after coordinate transformation read

$$\hat{\mathbf{U}}'_t + \hat{\mathbf{F}}'^c_\xi + \hat{\mathbf{G}}'^c_\eta + \hat{\mathbf{H}}'^c_\zeta = \hat{\mathbf{F}}'^v_\xi + \hat{\mathbf{G}}'^v_\eta + \hat{\mathbf{H}}'^v_\zeta, \tag{2.55}$$

where

$$\hat{\mathbf{U}}' = \frac{\mathbf{U}'}{J} \tag{2.56}$$

$$\hat{\mathbf{F}}'^c = \frac{1}{J}(\xi_x \mathbf{F}'^c + \xi_y \mathbf{G}'^c + \xi_z \mathbf{H}'^c) \tag{2.57}$$

$$\hat{\mathbf{G}}'^c = \frac{1}{J}(\eta_x \mathbf{F}'^c + \eta_y \mathbf{G}'^c + \eta_z \mathbf{H}'^c) \tag{2.58}$$

$$\hat{\mathbf{H}}'^c = \frac{1}{J}(\zeta_x \mathbf{F}'^c + \zeta_y \mathbf{G}'^c + \zeta_z \mathbf{H}'^c) \tag{2.59}$$

$$\hat{\mathbf{F}}'^v = \frac{1}{J}(\xi_x \mathbf{F}'^v + \xi_y \mathbf{G}'^v + \xi_z \mathbf{H}'^v) \tag{2.60}$$

$$\hat{\mathbf{G}}'^v = \frac{1}{J}(\eta_x \mathbf{F}'^v + \eta_y \mathbf{G}'^v + \eta_z \mathbf{H}'^v) \tag{2.61}$$

$$\hat{\mathbf{H}}'^{v} = \frac{1}{J}(\zeta_x \mathbf{F}'^{v} + \zeta_y \mathbf{G}'^{v} + \zeta_z \mathbf{H}'^{v}) \tag{2.62}$$

2.2.1 Coordinate transformation in code

The coordinate transformation enters the program code is in subroutines called METRIC_NUMERI and METRIC_JACOBI. The relations described in equations (2.41) – (2.52) are coded in METRIC_NUMERI. METRIC_JACOBI is a short subroutine for computing the Jacobian determinant (eq. 2.53).

2.3 Physical boundary conditions

The boundary conditions are established for the physical domain. In this case 3 different types are used: periodic, adiabatic no-slip and non-reflecting characteristic boundary conditions. Only the adiabatic no-slip boundary conditions are outlined here, while the other two conditions are described in chapter 3, which deals with the numerical solution. The domain is shown in Figure 2.2 for better orientation in this problem. This domain arrangement is used for verification with the existing 2D version of the code.

2.3.1 Adiabatic no-slip boundary conditions

The no-slip boundary condition implies zero velocity the walls. Adiabatic walls allow no heat conduction. The boundary conditions at an adiabatic no-slip wall are

$$u = v = w = 0 \tag{2.63}$$

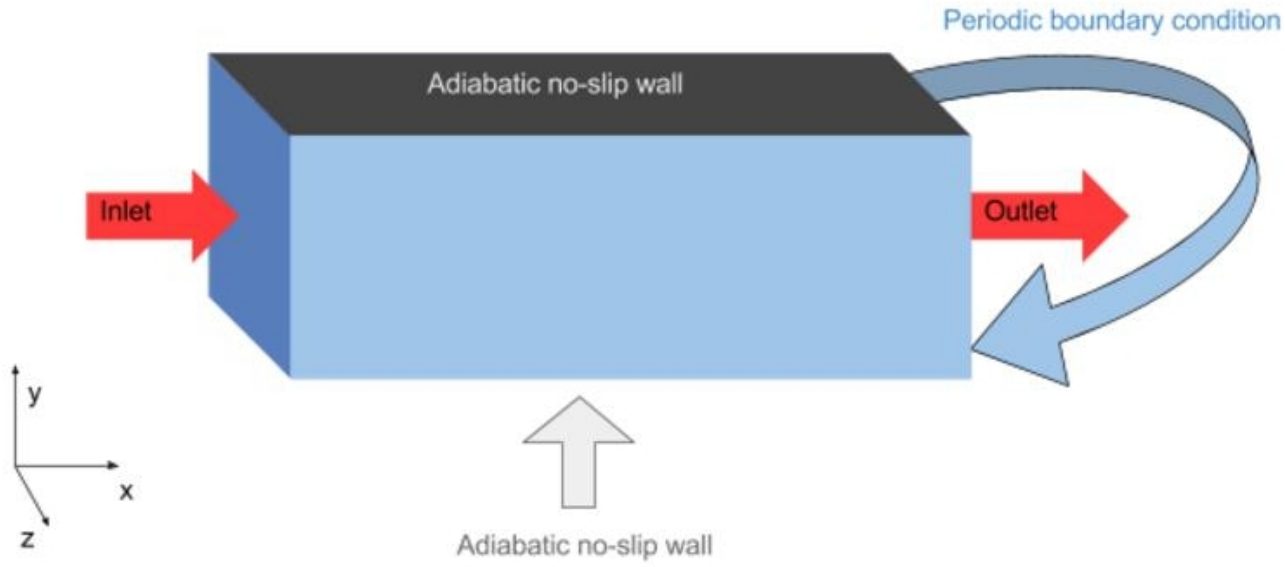

Figure 2.2: Computational domain with boundary conditions

and

$$\frac{dT}{dy} = 0. \tag{2.64}$$

A special approach is used for the pressure computation. It is computed directly from Navier-Stokes equations and no assumption is made. The relation for the dimensionless perturbation pressure is described in equation (2.37). Based on this pressure perturbation the dimensionless perturbation density at the wall is computed from

$$\rho' = \frac{\gamma p' - T'}{1 + T'}. \tag{2.65}$$

2.3.2 Inlet and outlet boundary conditions

The velocity value is prescribed at the inlet and the pressure value is entered at the outlet. As mentioned above, non-reflecting characteristic boundary conditions used at inlet and outlet are described in chapter 3.

Chapter 3

Numerical solution

The Navier-Stokes equations (3.46) are discretized by different types of discretizations for temporal and spatial parts of the equations. These discretizations are described in sections 3.1 and 3.2 below. The standard Runge-Kutta method is used for the discretization in time and 6^{th} order discretization schemes are used to approximate the spatial derivatives in the interior and 3^{th} order schemes are used at the boundary for space discretization. The summation by parts (SBP) operator is used for the spatial derivative.

3.1 Discretization in time

The standard Runge-Kutta method is used for finding numerical solution for the Navier-Stokes equations in time. The spatial derivatives are approximated in each of the 4 Runge-Kutta stages, which are

$$k_1 = \Delta t \mathbf{R}(\mathbf{U'}^n), \tag{3.1}$$

$$k_2 = \Delta t \mathbf{R}(\mathbf{U'}^n + c_2 k_1), \tag{3.2}$$

$$k_3 = \Delta t \mathbf{R}(\mathbf{U'}^n + c_3 k_2), \tag{3.3}$$

$$k_4 = \Delta t \mathbf{R}(\mathbf{U'}^n + c_4 k_3), \tag{3.4}$$

$$\mathbf{U'}^{n+1} = \mathbf{U'}^n + b_1 k_1 + b_2 k_2 + b_3 k_3 + b_4 k_4, \tag{3.5}$$

where $\mathbf{R}(\mathbf{U'})$ is residuals vector and $\mathbf{U'}$ is defined in (2.2). The time step Δt is applied in subroutine RESIDUAL, where each of the residuals is multiplied by the time step and divided by the cell volume.

The values of the coefficients b_i are written in table 3.1.

Coefficient b_i	Value
b_1	1/6
b_2	1/3
b_3	1/3
b_4	1/6

Table 3.1: Coefficients b_i for 4 stages of the Runge-Kutta scheme

The second parameter c_i is used in different stages of the Runge-Kutta method and its values are shown in table 3.2.

Coefficient c_i	Value
c_2	1/2
c_3	1/2
c_4	1

Table 3.2: Coefficients c_i for 4 stages of the Runge-Kutta scheme

The time derivative in the Navier-Stokes equation is calculated as

$$\hat{\mathbf{U}}'_t = \mathbf{R}(\mathbf{U}), \tag{3.6}$$

where $\mathbf{R}(\mathbf{U})$ are residuals, which are functions of the Conservative variables. $\mathbf{U'}$ is defined in equation (2.2), $\mathbf{U'}_t$ is from Navier-Stokes equations (3.46) and resid-

uals are the rest of the same equations.

3.1.1 Time discretization in the code

Several subroutines are used to evaluate the time derivative. They are listed below with their main functions.

SAVEA saves the previous solution, it is placed before Runge-Kutta (RK) stages

SWEEPA does 4 stages of RK, subroutines listed below called from this subroutine

RESIDUAL calculates residuals

BOUNDV corrects solution for adiabatic no-slip wall

STOREQ saves solution between stages of RK

FILCET 6^{th} order filter in η direction

FILCXSI 6^{th} order filter in ξ direction

FILET 6^{th} order filter in ζ direction

STOREF saves solution after filtration

3.2 Discretization in space

Discretization in space is made by the summation by parts operator **Q** defined by [2] with 6^{th} order accuracy in the interior and 3^{rd} order near boundaries. This accuracy is accomplished by special coefficients q_{ij}.

$$Q = \begin{pmatrix} q_{11} & q_{12} & q_{13} & q_{14} & q_{15} & 0 & 0 & 0 & 0 & \dots \\ q_{21} & 0 & q_{23} & q_{24} & q_{25} & q_{26} & 0 & 0 & 0 & \dots \\ q_{31} & q_{32} & 0 & q_{34} & q_{35} & q_{36} & 0 & 0 & 0 & \dots \\ q_{41} & q_{42} & q_{43} & 0 & q_{45} & q_{46} & q_{47} & 0 & 0 & \dots \\ q_{51} & q_{52} & q_{53} & q_{54} & 0 & q_{56} & q_{57} & q_{58} & 0 & \dots \\ 0 & q_{62} & q_{63} & q_{64} & q_{65} & 0 & q_{67} & q_{68} & q_{69} & 0\dots \\ 0 & 0 & \frac{-1}{60} & \frac{9}{60} & \frac{-45}{60} & 0 & \frac{45}{60} & \frac{-9}{60} & \frac{1}{60} & 0\dots \\ \vdots & & & & & \ddots & & & & \vdots \\ & & & \dots & & & & & & q_{ij} \end{pmatrix}, \tag{3.7}$$

where i goes from 1 to 6 and j goes from 1 to 9 and values of q_{ij} are listed in table 3.3

q_{11}	-1.5825335189391164188	q_{45}	0.42710082726876904895
q_{12}	1.9968007424231323418	q_{46}	$-0.14377682403433476395e-1$
q_{13}	$0.00479888636530148728884e-2$	q_{47}	$0.13435342414629595074e-1$
q_{14}	-0.66986592424353432486	q_{51}	$-0.869154923617282383 31e-1$
q_{15}	0.25079981439421691455	q_{52}	0.29554398882823409928
q_{21}	-0.45374732928216654180	q_{53}	-0.23775972239854428505
q_{23}	0.20413995948833208469	q_{54}	-0.58114341331302103170
q_{24}	0.42505341435666916396	q_{56}	0.75652321103635055647
q_{25}	-0.19379006076750187297	q_{57}	-0.16452964326520248826
q_{26}	$0.183440162046671661 26e-1$	q_{58}	$0.18281071473911387584e-1$
q_{31}	$-0.241608262633714496 50e-2$	q_{62}	$-0.25155437851495019140e-1$
q_{32}	-0.45229312676749047092	q_{63}	$0.79610054564964270222e-1$
q_{34}	0.23791958686831427518	q_{64}	$0.17590922581676217438e-1$
q_{35}	0.34541374646501905816	q_{65}	-0.68025083141176381057
q_{36}	-0.12862412393950571745	q_{67}	0.73970913906075203762
q_{41}	0.17061018846799776078	q_{68}	-0.14794182781215040752
q_{42}	-0.47641039995023947254	q_{69}	$0.16437980868016711947e-1$
q_{43}	-0.12035827579772345587		

Table 3.3: Coefficients q_{ij} for summation by parts operator Q [2]

This operator is used for all spatial derivatives except for derivatives for direc-

tions where the periodic boundary is applied. More about this boundary condition can be found in subsection 3.4.1 Periodic boundary condition.

3.3 Stability of numerical solution

Two ways how to select time step are implemented in the code. The first one is a fixed time step Δt. The second one is a time step Δt dependent on the Courant-Friedrichs-Lewy condition number (CFL) and the von Neumann number (VNN). As described in [16] the Courant-Friedrichs-Lewy and von Neumann numbers are defined as

$$CFL = \Delta t\left(\frac{|U^{(\xi)}|}{\Delta\xi} + \frac{|U^{(\eta)}|}{\Delta\eta} + \frac{|U^{(\zeta)}|}{\Delta\zeta} + c\sqrt{\frac{|\bigtriangledown\xi|^2}{\Delta\xi^2} + \frac{|\bigtriangledown\eta|^2}{\Delta\eta^2} + \frac{|\bigtriangledown\zeta|^2}{\Delta\zeta^2}}\right), \tag{3.8}$$

where $U^{(\xi)} = \frac{\partial\xi}{\partial t} + \mathbf{u}\cdot\bigtriangledown\xi$, $U^{(\eta)} = \frac{\partial\eta}{\partial t} + \mathbf{u}\cdot\bigtriangledown\eta$, $U^{(\zeta)} = \frac{\partial\zeta}{\partial t} + \mathbf{u}\cdot\bigtriangledown\zeta$, $\bigtriangledown = \left(\frac{\partial}{\partial x}, \frac{\partial}{\partial y}, \frac{\partial}{\partial z}\right)^T$ and

$$VNN = \Delta t \cdot max\left(\frac{4}{3}\frac{\mu}{\rho}, \frac{\gamma\mu}{\rho Pr}\right)\cdot\left(\left(\frac{\bigtriangledown\xi}{\Delta\xi}\right)^2 + \left(\frac{\bigtriangledown\eta}{\Delta\eta}\right)^2 + \left(\frac{\bigtriangledown\zeta}{\Delta\zeta}\right)^2\right). \tag{3.9}$$

The CFL condition is in the program divided according to the transformed coordinates, and results are shown in every direction separately. For correct results, Courant number should not be bigger than 1. VNN should not be bigger than 0.5. This formula is also divided into three directions and results are shown in every direction as well.

3.4 Numerical boundary conditions

Two types of boundary conditions are chosen for numerical purposes: periodic and non-reflecting characteristic boundary conditions. They are described in subsections below (3.4.1 and 3.4.2).

3.4.1 Periodic boundary conditions

Periodic boundary conditions are assumed in the z-direction, i. e. periodic boundary conditions

$$U'(x, y, z, t) = U'(x, y, z + z_p, t), \tag{3.10}$$

where z_p is the period. The idea of the numerical implementation is shown in the figure 3.1.

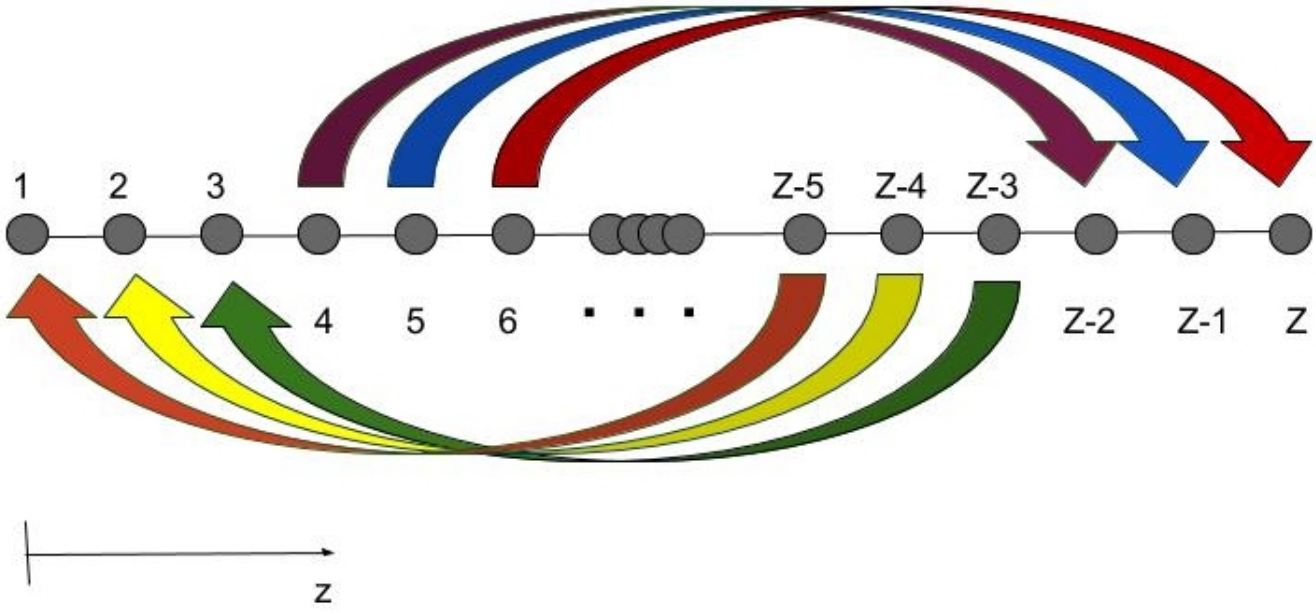

Figure 3.1: Numerical implementation of periodic boundary condition

An equidistant grid in the ζ-direction with grid spacing $\Delta\zeta = 1$ is assumed, where

Z is the number of grid points in the z-direction. We have $z_4 = 0$ and $z_{Z-2} = z_p$. Only $U'_{i,j,k}$ for $k = 4,\ldots,Z-3$ needs to be computed, because the periodic boundary condition implies $U'_{i,j,3} = U'_{i,j,Z-3}$.

Three overlapping points are used, because in this code a 6^{th} order finite difference method with a 7-point stencil is used, i. e. 3 points to the left and right of each point. Note that the grid points z_1, z_2, z_3, z_{Z-2}, z_{Z-1}, z_Z are periodically extending the domain as illustrated in Fig. 3.1.

Thus, a special subroutine is used for the approximation of the derivatives in ζ-direction. E. g. u_ζ is approximated by

$$D_\zeta u_{i,j,k} = \frac{1}{60}(-u_{i,j,k-3} + 9u_{i,j,k-2} - 45u_{i,j,k-1} + 45u_{i,j,k+1} - 9u_{i,j,k+2} + u_{i,j,k+3}). \tag{3.11}$$

Since the transformed viscous flux vector in the ζ-direction $\hat{\mathbf{H}}'^{\nu}$ contains ζ-derivatives computed at $k = 4,\ldots,Z-3$, we apply the same treatment described above, cf. Fig 3.1 to $\hat{\mathbf{H}}'^{\nu}$ before approximating $\hat{\mathbf{H}}'^{\nu}_{\zeta}$ similar to (3.11).

3.4.2 Non-reflecting characteristic boundary conditions

According to [17] non-reflecting boundary conditions can be used at inlet and outlet to reduce the reflection of acoustic waves, when numerical methods are implemented.

The non-reflecting boundary conditions by [17] are called Navier-Stokes characteristic boundary conditions (NSCBC) and target direct numerical simulation of turbulent flows. But they are also suitable for low Reynolds number flow.

The vector **d** introduced by [18] is given by characteristic analysis and for transformed coordinates is given as

$$\begin{bmatrix} d_1 \\ d_2 \\ d_3 \\ d_4 \\ d_5 \end{bmatrix} := \begin{bmatrix} \mathscr{L}_2 + \frac{|\hat{\xi}|}{c} \cdot (\mathscr{L}_5 - \mathscr{L}_1) \\ \frac{\hat{\eta}_x}{|\nabla\hat{\eta}|}\mathscr{L}_3 + \frac{\hat{\zeta}_x}{|\nabla\hat{\zeta}|}\mathscr{L}_4 + \frac{\hat{\xi}_x}{\rho}(\mathscr{L}_5 + \mathscr{L}_1) \\ \frac{\hat{\eta}_y}{|\nabla\hat{\eta}|}\mathscr{L}_3 + \frac{\hat{\zeta}_y}{|\nabla\hat{\zeta}|}\mathscr{L}_4 + \frac{\hat{\xi}_y}{\rho}(\mathscr{L}_5 + \mathscr{L}_1) \\ \frac{\hat{\eta}_z}{|\nabla\hat{\eta}|}\mathscr{L}_3 + \frac{\hat{\zeta}_z}{|\nabla\hat{\zeta}|}\mathscr{L}_4 + \frac{\hat{\xi}_z}{\rho}(\mathscr{L}_5 + \mathscr{L}_1) \\ c \cdot |\hat{\xi}| \cdot (\mathscr{L}_5 - \mathscr{L}_1) \end{bmatrix}, \tag{3.12}$$

where $\mathscr{L}_1, \mathscr{L}_2, \mathscr{L}_3, \mathscr{L}_4, \mathscr{L}_5$ are given below in eq. 3.30.

Poinsot and Lele's [17] characteristic boundary conditions are based on Local One-Dimensional Inviscid (LODI) relations and in transformed coordinates they are described as

$$J^{-1} \cdot \begin{pmatrix} 1 & 0 & 0 & 0 & 0 \\ 0 & \rho & 0 & 0 & 0 \\ 0 & 0 & \rho & 0 & 0 \\ 0 & 0 & 0 & \rho & 0 \\ 0 & 0 & 0 & 0 & \frac{1}{\gamma-1} \end{pmatrix} \cdot \begin{pmatrix} \rho_t \\ u_t \\ v_t \\ w_t \\ p_t \end{pmatrix} + \begin{pmatrix} U & \rho\hat{\xi}_x & \rho\hat{\xi}_y & \rho\hat{\xi}_z & 0 \\ 0 & U\rho & 0 & 0 & \hat{\xi}_x \\ 0 & 0 & U\rho & 0 & \hat{\xi}_y \\ 0 & 0 & 0 & U\rho & \hat{\xi}_z \\ 0 & \frac{\gamma p}{\gamma-1}\hat{\xi}_x & \frac{\gamma p}{\gamma-1}\hat{\xi}_y & \frac{\gamma p}{\gamma-1}\hat{\xi}_z & U\frac{1}{\gamma-1} \end{pmatrix} \cdot \begin{pmatrix} \rho_\xi \\ u_\xi \\ v_\xi \\ w_\xi \\ p_\xi \end{pmatrix} = 0, \tag{3.13}$$

where

$$U = \hat{\xi}_x u + \hat{\xi}_y v + \hat{\xi}_z w \tag{3.14}$$

and the second matrix is labeled as **B** and the vector that multiplies **B** is named $\mathbf{V}_\xi$. In this system the $\hat{\eta}$- and $\hat{\zeta}$- derivatives are neglected. For the LODI system

the following equation is also valid

$$J^{-1}\cdot\begin{bmatrix}\rho\\ u\\ v\\ w\\ p\end{bmatrix}_t+\begin{bmatrix}d_1\\ d_2\\ d_3\\ d_4\\ d_5\end{bmatrix}=0. \tag{3.15}$$

The columns of the matrix **R** are defined by the eigenvectors of the matrix **B**. The eigenvalues of **R** are determined by

$$det(\mathbf{B}-\lambda\mathbf{I})=0, \tag{3.16}$$

i. e.

$$\begin{vmatrix} U-\lambda & \rho\hat{\xi}_x & \rho\hat{\xi}_y & \rho\hat{\xi}_z & 0\\ 0 & U-\lambda & 0 & 0 & \frac{\hat{\xi}_x}{\rho}\\ 0 & 0 & U-\lambda & 0 & \frac{\hat{\xi}_y}{\rho}\\ 0 & 0 & 0 & U-\lambda & \frac{\hat{\xi}_z}{\rho}\\ 0 & \gamma p\hat{\xi}_x & \gamma p\hat{\xi}_y & \gamma p\hat{\xi}_z & U-\lambda \end{vmatrix} = \left(U-\lambda\right)^2\cdot\left[\left(U-\lambda\right)^3-\left(U-\lambda\right)\cdot c^2\left(\hat{\xi}_x{}^2+\hat{\xi}_y{}^2+\hat{\xi}_z{}^2\right)\right]=0 \tag{3.17}$$

Thus, the eigenvalues of **B** are

$$\lambda_1=U-c\sqrt{\hat{\xi}_x{}^2+\hat{\xi}_y{}^2+\hat{\xi}_z{}^2}, \tag{3.18}$$

$$\lambda_2=\lambda_3=\lambda_4=U, \tag{3.19}$$

$$\lambda_5 = U + c\sqrt{\hat{\xi}_x{}^2 + \hat{\xi}_y{}^2 + \hat{\xi}_z{}^2}. \tag{3.20}$$

The eigenvectors corresponding to these eigenvalues are

$$v_1 = \begin{pmatrix} -\frac{|\hat{\xi}|}{c} & \frac{\hat{\xi}_x}{\rho} & \frac{\hat{\xi}_y}{\rho} & \frac{\hat{\xi}_z}{\rho} & -c\cdot|\hat{\xi}| \end{pmatrix}^T, \tag{3.21}$$

$$v_2 = \begin{pmatrix} 1 & 0 & 0 & 0 & 0 \end{pmatrix}^T, \tag{3.22}$$

$$v_3 = \begin{pmatrix} 0 & \frac{\hat{\eta}_x}{|\nabla\hat{\eta}|} & \frac{\hat{\eta}_y}{|\nabla\hat{\eta}|} & \frac{\hat{\eta}_z}{|\nabla\hat{\eta}|} & 0 \end{pmatrix}^T, \tag{3.23}$$

$$v_4 = \begin{pmatrix} 0 & \frac{\hat{\zeta}_x}{|\nabla\hat{\zeta}|} & \frac{\hat{\zeta}_y}{|\nabla\hat{\zeta}|} & \frac{\hat{\zeta}_z}{|\nabla\hat{\zeta}|} & 0 \end{pmatrix}^T, \tag{3.24}$$

$$v_5 = \begin{pmatrix} \frac{|\hat{\xi}|}{c} & \frac{\hat{\xi}_x}{\rho} & \frac{\hat{\xi}_y}{\rho} & \frac{\hat{\xi}_z}{\rho} & c\cdot|\hat{\xi}| \end{pmatrix}^T. \tag{3.25}$$

Thus the matrix **R** is

$$R = \begin{pmatrix} -\frac{|\hat{\xi}|}{c} & 1 & 0 & 0 & \frac{|\hat{\xi}|}{c} \\ \frac{\hat{\xi}_x}{\rho} & 0 & \frac{\hat{\eta}_x}{|\nabla\hat{\eta}|} & \frac{\hat{\zeta}_x}{|\nabla\hat{\zeta}|} & \frac{\hat{\xi}_x}{\rho} \\ \frac{\hat{\xi}_y}{\rho} & 0 & \frac{\hat{\eta}_y}{|\nabla\hat{\eta}|} & \frac{\hat{\zeta}_y}{|\nabla\hat{\zeta}|} & \frac{\hat{\xi}_y}{\rho} \\ \frac{\hat{\xi}_z}{\rho} & 0 & \frac{\hat{\eta}_z}{|\nabla\hat{\eta}|} & \frac{\hat{\zeta}_z}{|\nabla\hat{\zeta}|} & \frac{\hat{\xi}_z}{\rho} \\ -c\cdot|\hat{\xi}| & 0 & 0 & 0 & c\cdot|\hat{\xi}| \end{pmatrix}. \tag{3.26}$$

The inverse of **R** is

$$R^{-1} = \begin{pmatrix} 0 & \frac{\rho}{2}\cdot\frac{\hat{\eta}_z\hat{\zeta}_y - \hat{\eta}_y\hat{\zeta}_z}{Q} & \frac{\rho}{2}\cdot\frac{\hat{\eta}_x\hat{\zeta}_z - \hat{\eta}_z\hat{\zeta}_x}{Q} & \frac{\rho}{2}\cdot\frac{\hat{\eta}_y\hat{\zeta}_x - \hat{\eta}_x\hat{\zeta}_y}{Q} & \frac{-1}{2c|\xi|} \\ 1 & 0 & 0 & 0 & \frac{-1}{c^2} \\ 0 & |\nabla\eta|\cdot\frac{\hat{\xi}_y\hat{\zeta}_z - \hat{\xi}_z\hat{\zeta}_y}{Q} & |\nabla\eta|\cdot\frac{\hat{\xi}_x\hat{\zeta}_z - \hat{\xi}_z\hat{\zeta}_x}{Q} & |\nabla\eta|\cdot\frac{\hat{\xi}_x\hat{\zeta}_y - \hat{\xi}_y\hat{\zeta}_x}{Q} & 0 \\ 0 & |\nabla\zeta|\cdot\frac{\hat{\xi}_z\hat{\eta}_y - \hat{\xi}_y\hat{\eta}_z}{Q} & |\nabla\zeta|\cdot\frac{\hat{\xi}_x\hat{\eta}_z - \hat{\xi}_z\hat{\eta}_x}{Q} & |\nabla\zeta|\cdot\frac{\hat{\xi}_y\hat{\eta}_x - \hat{\xi}_x\hat{\eta}_y}{Q} & 0 \\ 0 & \frac{\rho}{2}\cdot\frac{\hat{\eta}_z\hat{\zeta}_y - \hat{\eta}_y\hat{\zeta}_z}{Q} & \frac{\rho}{2}\cdot\frac{\hat{\eta}_x\hat{\zeta}_z - \hat{\eta}_z\hat{\zeta}_x}{Q} & \frac{\rho}{2}\cdot\frac{\hat{\eta}_y\hat{\zeta}_x - \hat{\eta}_x\hat{\zeta}_y}{Q} & \frac{1}{2c|\xi|} \end{pmatrix}, \tag{3.27}$$

where

$$Q = \hat{\xi}_x(\hat{\eta}_z\hat{\zeta}_y - \hat{\eta}_y\hat{\zeta}_z) + \hat{\eta}_x(\hat{\xi}_y\hat{\zeta}_z - \hat{\xi}_z\hat{\zeta}_y) + \hat{\zeta}_x(\hat{\eta}_y\hat{\xi}_z - \hat{\eta}_z\hat{\xi}_y). \tag{3.28}$$

As the vector $\mathscr{L}$ is defined by

$$\mathscr{L} = \mathbf{R}^{-1} \cdot \mathbf{V}_\xi, \tag{3.29}$$

its components are given by

$$\begin{bmatrix} \mathscr{L}_1 \\ \mathscr{L}_2 \\ \mathscr{L}_3 \\ \mathscr{L}_4 \\ \mathscr{L}_5 \end{bmatrix} = \begin{bmatrix} u_\xi \cdot \frac{\rho}{2} \cdot \frac{\hat{\eta}_z\hat{\zeta}_y - \hat{\eta}_y\hat{\zeta}_z}{Q} + v_\xi \cdot \frac{\rho}{2} \cdot \frac{\hat{\eta}_x\hat{\zeta}_z - \hat{\eta}_z\hat{\zeta}_x}{Q} + w_\xi \cdot \frac{\rho}{2} \cdot \frac{\hat{\eta}_y\hat{\zeta}_x - \hat{\eta}_x\hat{\zeta}_y}{Q} - \frac{p_\xi}{2c|\xi|} \\ \rho_\xi - \frac{p_\xi}{c^2} \\ u_\xi \cdot |\bigtriangledown\eta| \cdot \frac{\hat{\xi}_y\hat{\zeta}_z - \hat{\xi}_z\hat{\zeta}_y}{Q} + v_\xi \cdot |\bigtriangledown\eta| \cdot \frac{\hat{\xi}_x\hat{\zeta}_z - \hat{\xi}_z\hat{\zeta}_x}{Q} + w_\xi \cdot |\bigtriangledown\eta| \cdot \frac{\hat{\xi}_x\hat{\zeta}_y - \hat{\xi}_y\hat{\zeta}_x}{Q} \\ u_\xi \cdot |\bigtriangledown\zeta| \cdot \frac{\hat{\xi}_z\hat{\eta}_y - \hat{\xi}_y\hat{\eta}_z}{Q} + v_\xi \cdot |\bigtriangledown\zeta| \cdot \frac{\hat{\xi}_x\hat{\eta}_z - \hat{\xi}_z\hat{\eta}_x}{Q} + w_\xi \cdot |\bigtriangledown\zeta| \cdot \frac{\hat{\xi}_y\hat{\eta}_x - \hat{\xi}_x\hat{\eta}_y}{Q} \\ u_\xi \cdot \frac{\rho}{2} \cdot \frac{\hat{\eta}_z\hat{\zeta}_y - \hat{\eta}_y\hat{\zeta}_z}{Q} + v_\xi \cdot \frac{\rho}{2} \cdot \frac{\hat{\eta}_x\hat{\zeta}_z - \hat{\eta}_z\hat{\zeta}_x}{Q} + w_\xi \cdot \frac{\rho}{2} \cdot \frac{\hat{\eta}_y\hat{\zeta}_x - \hat{\eta}_x\hat{\zeta}_y}{Q} + \frac{p_\xi}{2c|\xi|} \end{bmatrix}. \tag{3.30}$$

The physical meaning of $\mathscr{L}_i$ can be found by looking at the linearized 1D Euler equations for one-dimensional inviscid acoustic waves. The amplitude A_1 is given by

$$A_1 = p' - \rho c u' \tag{3.31}$$

and it is associated with $(\mathbf{R}^{-1}v)_1$. And $\mathscr{L}_1$ represents the time variation of the wave amplitude A_1 as the rest of $\mathscr{L}_i$ represent the A_i amplitudes.

3.4.3 Inflow

These values are imposed at the inlet

$$u(0, y, z) = u_{in}(y, z), \tag{3.32}$$

$$v(0,y,z) = 0, \tag{3.33}$$

$$w(0,y,z) = 0, \tag{3.34}$$

$$T(0,y,z) = T_{in}(y,z). \tag{3.35}$$

$\rho(0,y,z)$ is computed at the inlet boundary from the continuity equation with respect to acoustics waves using $\mathscr{L}_1$. The imposed conditions at the inlet give

$$\mathscr{L}_3 = \mathscr{L}_4 = 0, \tag{3.36}$$

$$\mathscr{L}_5 = -\mathscr{L}_1, \tag{3.37}$$

$$\mathscr{L}_2 = -2(\gamma-1)\frac{|\hat{\xi}|}{c}\mathscr{L}_1 \tag{3.38}$$

so d_1 (eq. 3.12) is

$$d_1 = \mathscr{L}_2 + \frac{|\hat{\xi}|}{c}\cdot(\mathscr{L}_5 - \mathscr{L}_1) = -2\gamma\frac{|\hat{\xi}|}{c}\mathscr{L}_1 \tag{3.39}$$

and the continuity equation from which ρ at the inlet is computed is

$$J^{-1}\rho_t + d_1 + \rho u(\hat{\xi}_x)_\xi + \rho v(\hat{\xi}_y)_\xi + \rho w(\hat{\xi}_z)_\xi + [\rho u\hat{\eta}_x + \rho v\hat{\eta}_y + \rho w\hat{\eta}_z]_\eta + [\rho u\hat{\zeta}_x + \rho v\hat{\zeta}_y + \rho w\hat{\zeta}_z]_\zeta = 0. \tag{3.40}$$

3.4.4 Outflow

The outflow boundary condition is supposed to impose an ingoing wave described by

$$\mathscr{L}_1 = K(p - p_\infty) + \mathscr{L}_1^{exact}, \tag{3.41}$$

where $\mathscr{L}_1^{exact}$ stands for exact value of $\mathscr{L}_1$ and it is called perfectly non-reflecting according to [18], its value is given in equation (3.44). K is a constant defined as

$$K = \sigma(1 - M^2)\frac{c}{L}, \tag{3.42}$$

where σ is constant ($\sigma = 0.25$) and M is the maximum Mach number in the flow, which is defined as

$$M = \frac{U_{max}}{c}. \tag{3.43}$$

$\mathscr{L}_1^{exact}$ in transformed coordinates is

$$\mathscr{L}_1^{exact} = \left(-\frac{U}{2c|\hat{\xi}|\xi_x} + \frac{1}{2\xi_x} \right) p_x^{exact} \cdot (-2c\xi_x), \tag{3.44}$$

where $-2c\xi_x$ is a scaling factor and p_x^{exact} is

$$p_x^{exact} = -2\mu\frac{U_{max}}{l^2}. \tag{3.45}$$

The rest of the $\mathscr{L}_i$ components (3.30) stay as written in the equation (3.30). Thus the Navier-Stokes equations at the outlet are computed as

$$\hat{\mathbf{U}}'_t + \mathbf{Q}d_i + \hat{\mathbf{F}}'^c_\xi + \hat{\mathbf{G}}'^c_\eta + \hat{\mathbf{H}}'^c_\zeta = \hat{\mathbf{F}}'^v_\xi + \hat{\mathbf{G}}'^v_\eta + \hat{\mathbf{H}}'^v_\zeta, \tag{3.46}$$

where $i \in \{1,2,3,4,5\}$ and

$$\mathbf{Q} = \begin{pmatrix} 1 & 0 & 0 & 0 & 0 \\ u & \rho & 0 & 0 & 0 \\ v & 0 & \rho & 0 & 0 \\ w & 0 & 0 & \rho & 0 \\ \frac{u^2+v^2+w^2}{2} & \rho u & \rho v & \rho w & \frac{1}{\gamma-1} \end{pmatrix}. \tag{3.47}$$

These inflow and outflow boundary conditions are parts of subroutine RESIDUAL. It changes directly the residuals at inlet and outlet. For the inlet, only residual DR for density is changed. For the outlet, all residual vector components are overwritten.

Chapter 4

Results

Various test cases were realized for checking for checking the 3D program. The first test is uniform flow. Verification was made for 3D channel flow by setting it corresponding to the 2D case. The next test was made with a discontinuity at the inlet which was used for grid refinement study. The last case was 3D channel flow with prescribed velocity components u_0 and w_0 at the inlet.

4.1 Uniform flow

The uniform flow test is based on initializing the whole channel by the same value and obtaining the same value after one time step. It is used as the first check of the converted 3D code. The reason for this test is to show that the terms for the numerical transformation , eq. (2.41) – (2.52), are correctly implemented. The simulation is initialized by a uniform velocity field

$$\mathbf{u} = (0.2, 0, 0)^T. \tag{4.1}$$

The uniform density and pressure perturbations are

$$\rho'(t=0)=0, \tag{4.2}$$

$$p'(t=0)=0. \tag{4.3}$$

The grid is equidistant and 21 points are used in each direction for each block of the grid. This test is made with four blocks with a wall placed in the middle of the y-direction. Each block is a part of the computational domain which is handled by a different processor in parallel. The Reynolds number and Mach number are

$$Re_{in}=\frac{\rho_0 u_{in} L}{\mu_0}=378 \tag{4.4}$$

and

$$M_{in}=\frac{u_{in}}{c_0}=0.2, \tag{4.5}$$

respectively, where $u_{in}=68.6\,ms^{-1}$. The boundary conditions are described in Fig. 2.2.

A result of this simulation is shown in Fig. 4.1, namely the x-component u of the velocity vector. The v and w velocities are equal to 0. After one time step, there are no changes in the channel, except for the vicinity of the walls, which means that the numerical terms are implemented correctly to reproduce uniform flow away from the vicinity of the walls for a Cartesian grid. Note that uniform flow was not assumed at the walls, where $\frac{du}{dy}\neq 0$. However, this part of the computational domain is not significant for this test case, in which uniform flow away from the vicinity of the walls is checked. The flow variables at the boundaries including the walls are determined by the boundary conditions. The results are

checked after one time step. The visualization of the simulation is made by the Open Source program Paraview.

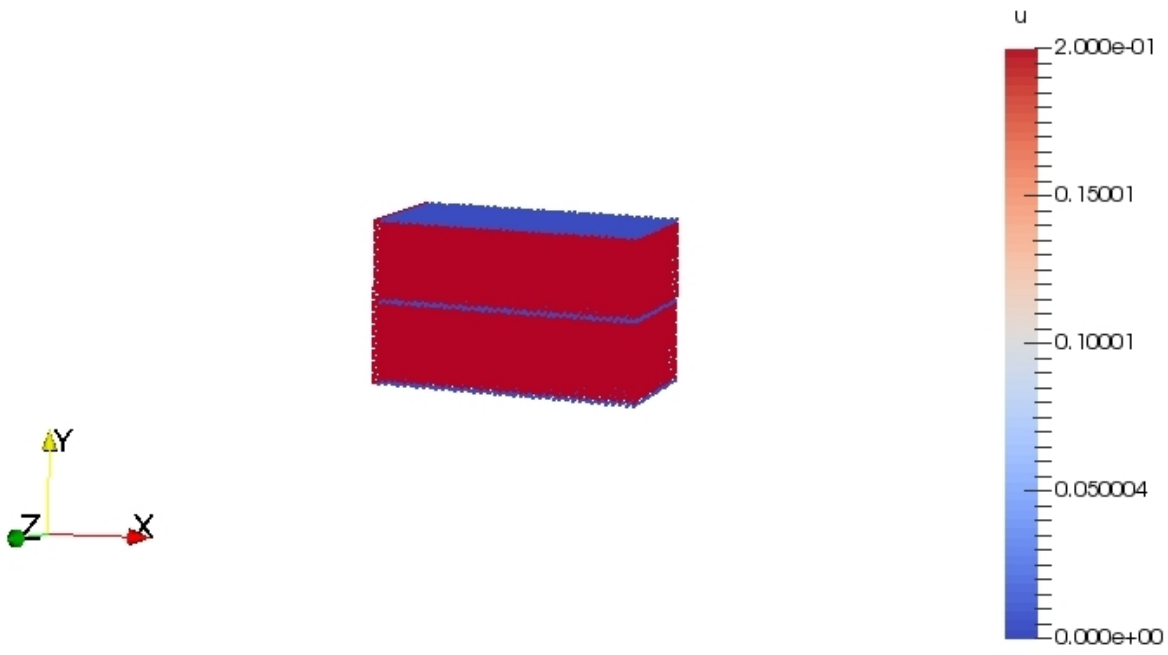

Figure 4.1: Simulation of uniform flow, velocity u

4.2 Reproduction of the 2D results with the 3D code

The purpose of this test case is to exactly reproduce the same solution as the one with the 2D program with the same initial conditions.

The 3D perturbation flow is simulated by the settings shown in Fig. 2.2. The non-reflecting numerical boundary conditions are used for inlet and outlet, the periodical boundary condition is applied in the z-direction. The physical boundary conditions of adiabatic walls are introduced in the y-direction. The boundary conditions at the inlet ($x = 0$) and the outlet ($x = 0.2$) are defined as

$$\mathbf{u}(0, y, z) = (M_{in}, 0, 0)^T, \tag{4.6}$$

$$T'(0, y, z) = 0, \tag{4.7}$$

$$p'(0.2, y, z) = 0, \tag{4.8}$$

where $M_{in} = 0.2$. The initial velocity vector is set to 0 in the whole domain except for the inlet. The Reynolds number is set as $Re_{in} = 378$. The grid is equidistant with 21 points in each directions. To be able to easily compare 2D and 3D cases Δz is set to 1. $\Delta x = 0.01$ and $\Delta y = 0.06$ for both cases.

Results are compared in the steady state. This state is obtained after approximately 10 000 time steps with $\Delta t = 5 \cdot 10^{-3}$. The development of the residuals for the 3D case is shown in Figure 4.2a for R_ρ, 4.2b for R_u, 4.2c for R_y, 4.2d for R_z and 4.2e for the energy residual R_E, where R_ρ, R_u, R_v, R_w and R_E are the components of the residual vector that is computed in each time step. The 2-norms of the residuals are scaled by dividing them by the 2-norms of the corresponding residuals at time level $n = 1$. The 2-norm of a residual component R_l^n is defined by

$$||R_l^n||_2 = \sqrt{\Delta x \cdot \Delta y \cdot \Delta z \cdot \sum_{i,j,k} R_{l_{i,j,k}}^2}. \tag{4.9}$$

Thus, we consider

$$\frac{||R_l^n||_2}{||R_l^1||_2}, \tag{4.10}$$

where $l \in \{\rho, u, v, w, E\}$.

The comparison of the 2D and 3D x-velocity contours is shown in Figures 4.3a for 2D and 4.3b for 3D results. The results in the x-y domain are the same in any plane normal to the z-direction. The middle plane ($k = 10$) was chosen for visualization in Figure 4.3b.

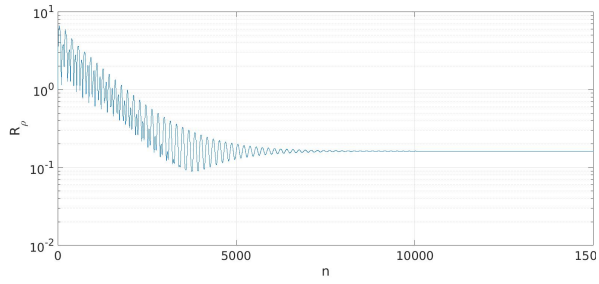

(a) ρ residual R_ρ

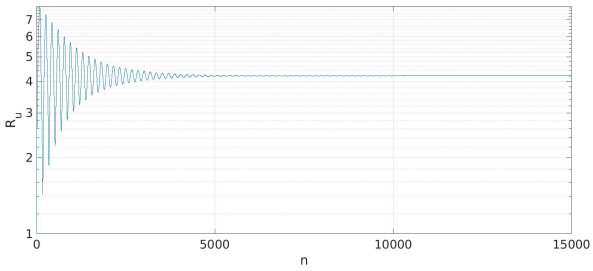

(b) ρu residual R_u

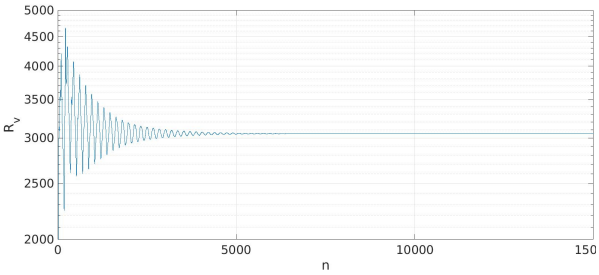

(c) ρv residual R_v

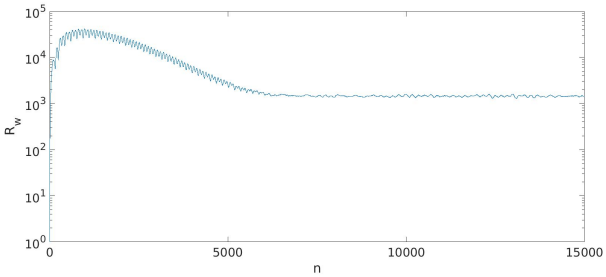

(d) ρw residual R_w

The velocity u in each plane $k \in \{1, \ldots, k_{max}\}$ was compared as

$$e_k = ||u_{3D_k} - u_{2D}||_2. \tag{4.11}$$

The error e_k was computed and its values are the same for each k, $e_k = 1.69 \cdot 10^{-8}$. The comparison of velocity profiles for $x = 0.15$ and $k = 10$ is shown in Fig. 4.4a and Fig. 4.4b. The profiles are almost the same for both 2D and 3D case with the

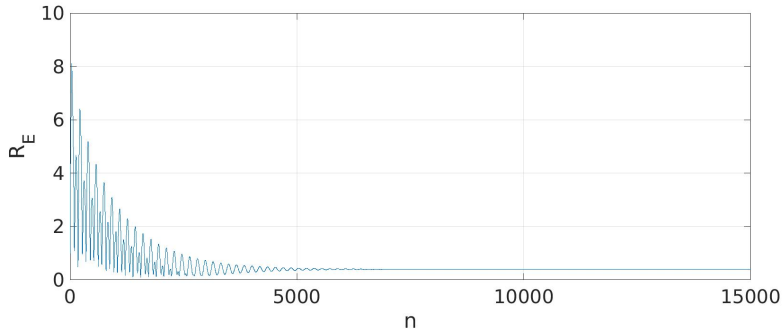

(e) Energy residual R_E

Figure 4.2: Plots of the 2-norms of the components of the residual vector

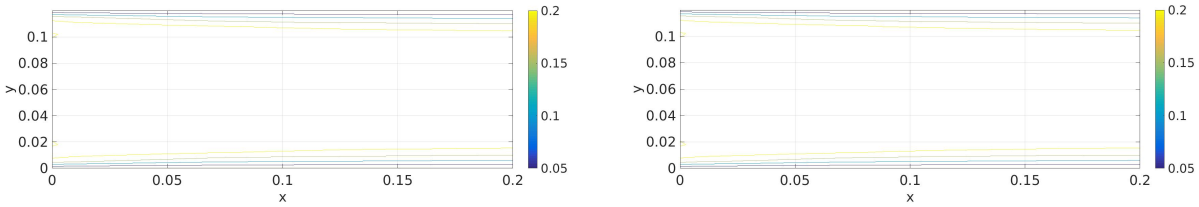

(a) 2D velocity u

(b) 3D velocity u, $k = 10$

Figure 4.3: Velocity u contours with $M_{in} = 0.2$, $Re_{in} = 378$ for 2D and 3D channel flow

maximum deviation below $2 \cdot 10^{-7}$.

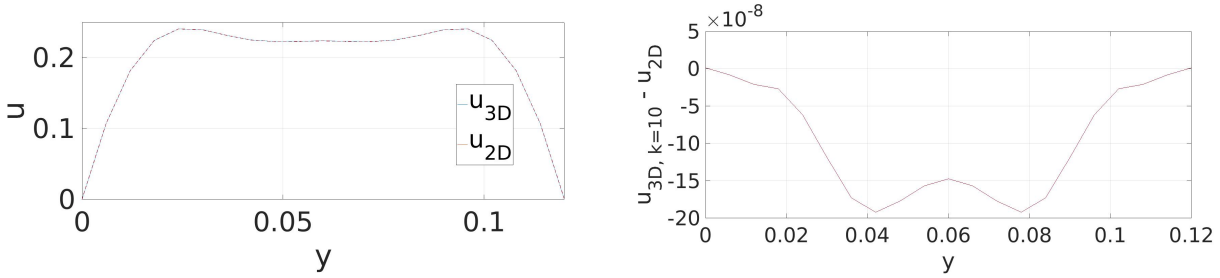

(a) 2D and 3D velocity profiles u for $x = 0.15$

(b) Comparison $u_{3D} - u_{2D}$, $k = 10$ for $x = 0.15$

Figure 4.4: Velocity u profile with $M_{in} = 0.2$, $Re_{in} = 378$ for 2D and 3D channel flow

Thus, the 2D results are accurately reproduced by the 3D code.

4.2.1 Rotation of the periodic and adiabatic no-slip boundary conditions

A rotation of the periodic and adiabatic no-slip boundary conditions was made. The periodic boundary conditions are introduced in the y-direction and the adiabatic no-slip boundary conditions are imposed in the z-direction. The Δy was set to 1 and $\Delta z = 0.06$. All others initial parameters stay as introduced in the test case in the beginning of this section 4.2.

The development of the residuals for the second 3D case is shown in Figure 4.2a for R_ρ, 4.5b for R_u, 4.5c for R_y, 4.5d for R_z and 4.5e for the energy residual R_E. All residuals Fig. 4.5a – 4.5e are the same as in the previous case with respect to axes rotation. e_k is computed as

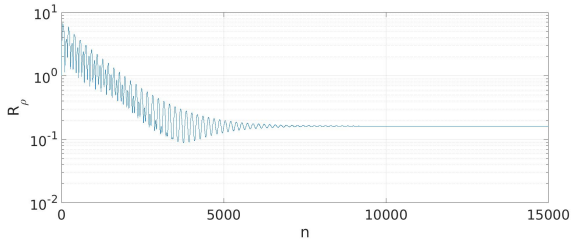

(a) ρ residual R_ρ

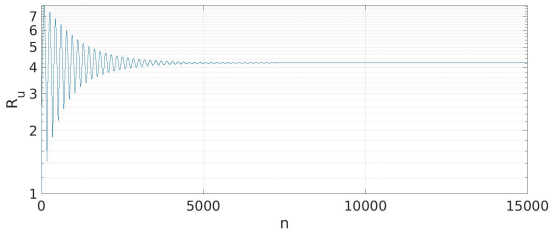

(b) ρu residual R_x

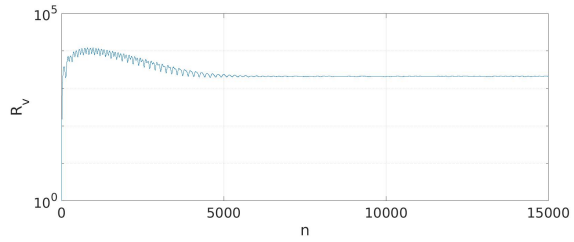

(c) ρv residual R_y

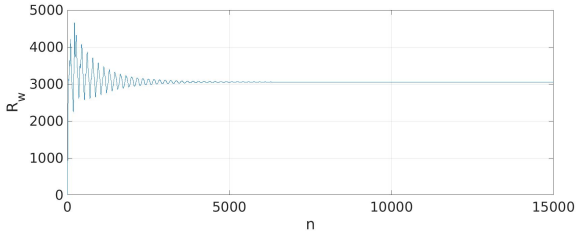

(d) ρw residual R_z

$$e_k = ||u_{1_k} - u_{2_k}||_2, \tag{4.12}$$

where $k \in \{1,2,\ldots,k_{max}\}$ and u_1 is the first test case, u_2 is the second one. The comparison for each k has the same results

$$e_{k_u} = ||u_{1_k} - u_{2_k}||_2 = \mathcal{O}(10^{-16}), \tag{4.13}$$

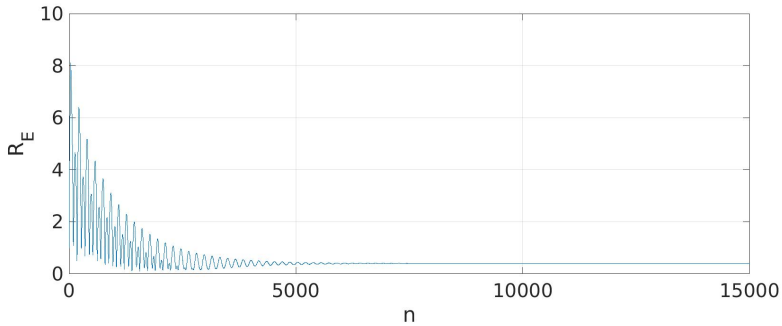

(e) Energy residual R_E

Figure 4.5: Plots of the 2-norm of the components of the residual vector for the second channel flow test with walls in z-direction and periodic boundary conditions in y-direction

$$e_{k_v} = ||v_{1_k} - w_{2_k}||_2 = \mathcal{O}(10^{-16}), \tag{4.14}$$

$$e_{k_w} = ||w_{1_k} - v_{2_k}||_2 = \mathcal{O}(10^{-16}). \tag{4.15}$$

4.3 Grid refinement study

The purpose of this study is to verify the influence of the computational grid on the results. Three simulations with different numbers of grid points are described.

The grid refinement study was performed for equidistant grids with $Re_{in} = 1000$ and $M_{in} = 0.5$. The time step Δt was decreased to 10^{-4} s on all grids to be able to obtain a stable computation. The final time of the simulations was 200 s. The velocity in the z-direction w_0 was introduced with a discontinuity. The initial conditions are

$$\rho_0' = 0, \tag{4.16}$$

$$p_0' = 0, \tag{4.17}$$

$$u_0 = M, \tag{4.18}$$

$$v_0 = 0, \tag{4.19}$$

$$w_0 = 0.01 \cdot u_0, \qquad k \in \{1, \ldots, \frac{k_{max} - 1}{2}\}, \tag{4.20}$$

and

$$w_0 = -0.01 \cdot u_0, \qquad k \in \{(k_{max} + 1)/2, \ldots, k_{max}\}. \tag{4.21}$$

The initial condition for w_0 is shown in Fig. 4.6. The grid refinement study is performed for 21, 41 and 61 grid points in each direction.

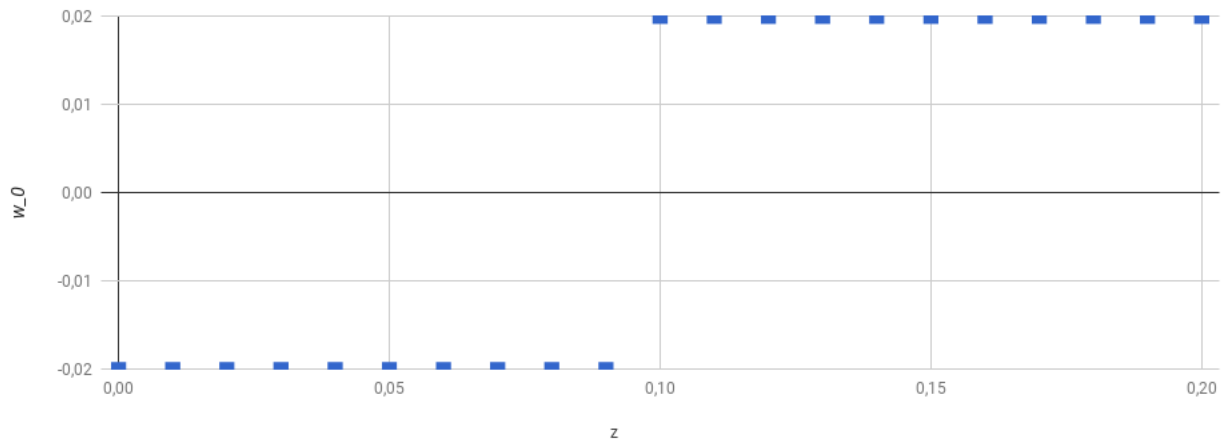

Figure 4.6: The initial values of w_0 along the z-axis

The convergence was checked for all of the cases used for the grid refinement study. The residuals results R_{u_i}, where $i \in \{21, 41, 61\}$ are shown in Fig. 4.7 – 4.9.

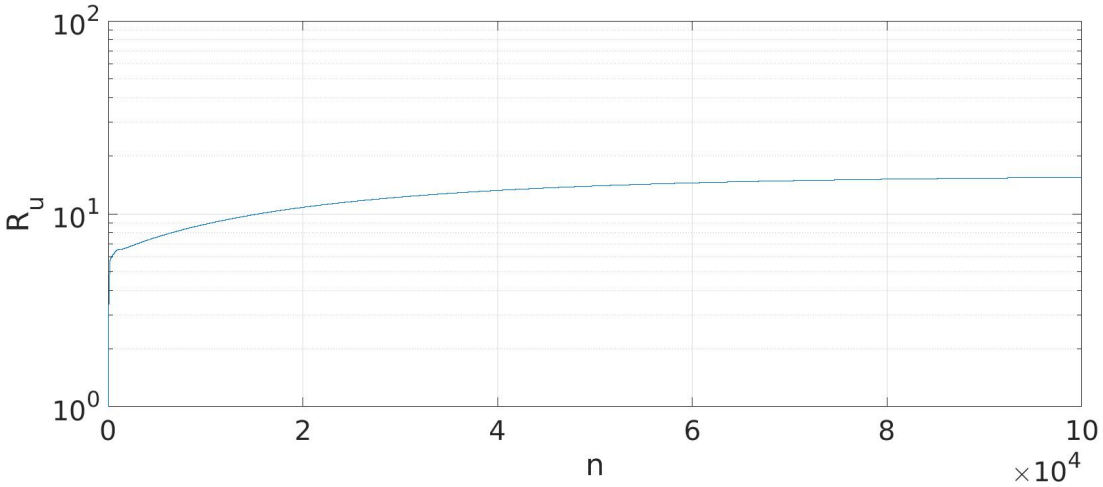

Figure 4.7: ρu residual R_u for 21 grid points for test with (4.16 – 4.21)

The results of the e_k norm are shown in Figure 4.10 for comparison between grids with 21 and 41 points and in Figure 4.11 for 41 and 61 points. The e_k norm is defined as

$$e_k = ||l_{g_k} - l_{(g+1)_k}||_2, \tag{4.22}$$

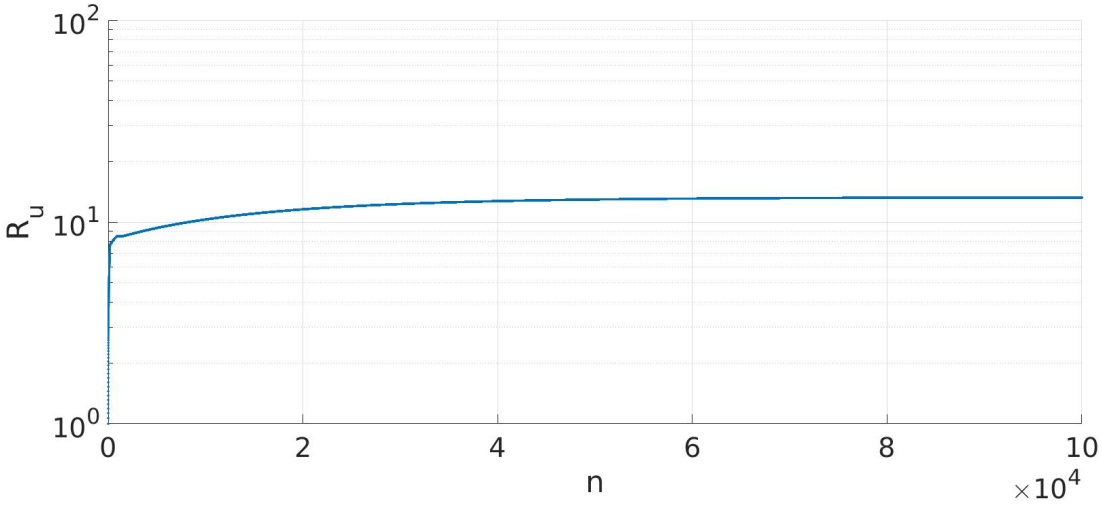

Figure 4.8: ρu residual R_u for 41 grid points for test with (4.16 – 4.21)

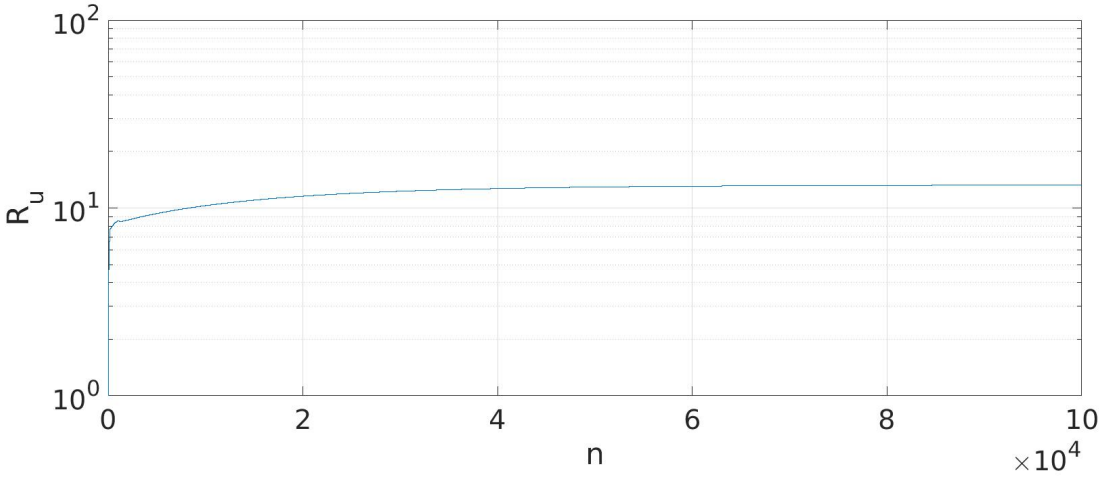

Figure 4.9: ρu residual R_u for 61 grid points for test with (4.16 – 4.21)

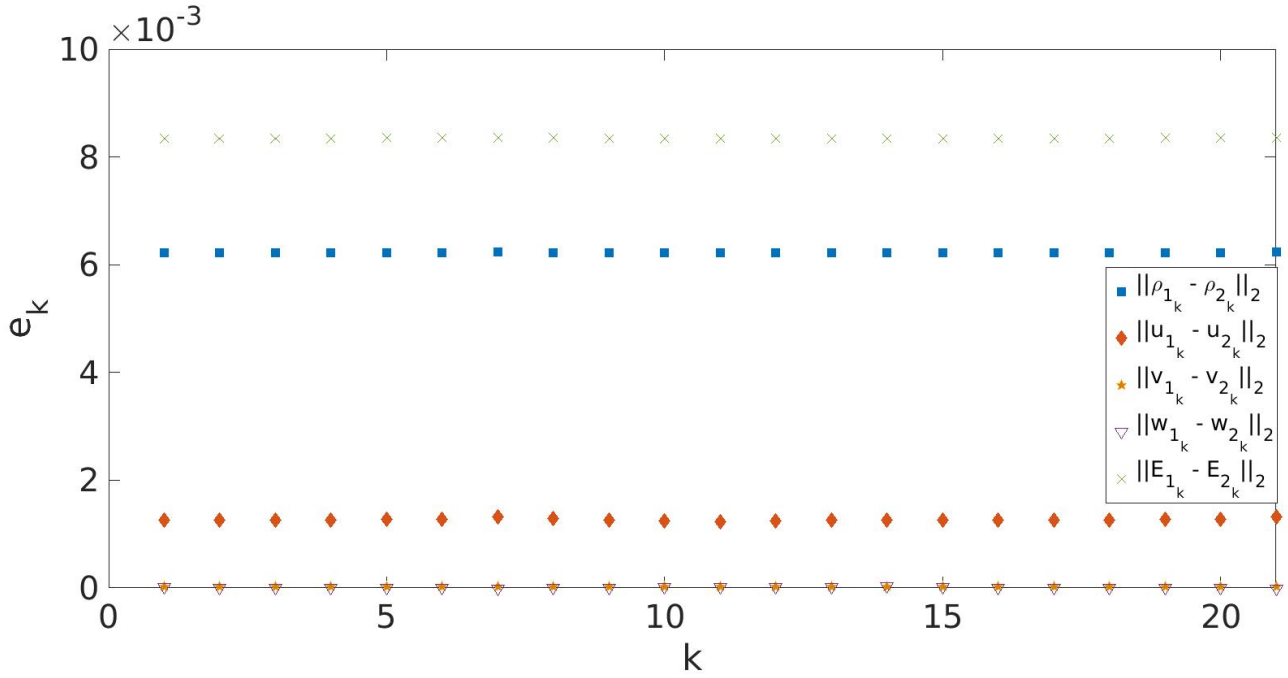

Figure 4.10: The comparison between grids with 21 and 41 points for test with (4.16 – 4.21)

where $l \in \{\rho, u, v, w, E\}$, $g = 1$ for 21, $g = 2$ for 41 and $g = 3$ for 61 points.

According to the e_k norm, the difference between the results with 21 and 41 grids points is quite high. The difference between 41 and 61 grid points has similar accuracy. Thus, for the current problem, the resolution of 41 grid points is recommended. The computational time grows fast with the number of grid points, for 21 points the CPU time was roughly 50 minutes, for 41 points 6 hours and for 61 points 10 hours. These tests were run on a personal computer. This code was not run in parallel.

The results of this simulations are shown for 41 grid points, Fig. 4.12a – 4.12i, which proved to be more accurate than 21 grids points. The planes xy, xz and yz are chosen with the value $i = \frac{i_{max}+1}{2}$ for the x-direction, $j = \frac{j_{max}+1}{2}$ for the y-direction and $k = \frac{k_{max}+1}{2}$ for the z-direction.

The discontinuity influence can be seen in Fig. 4.12a, where the velocity profile

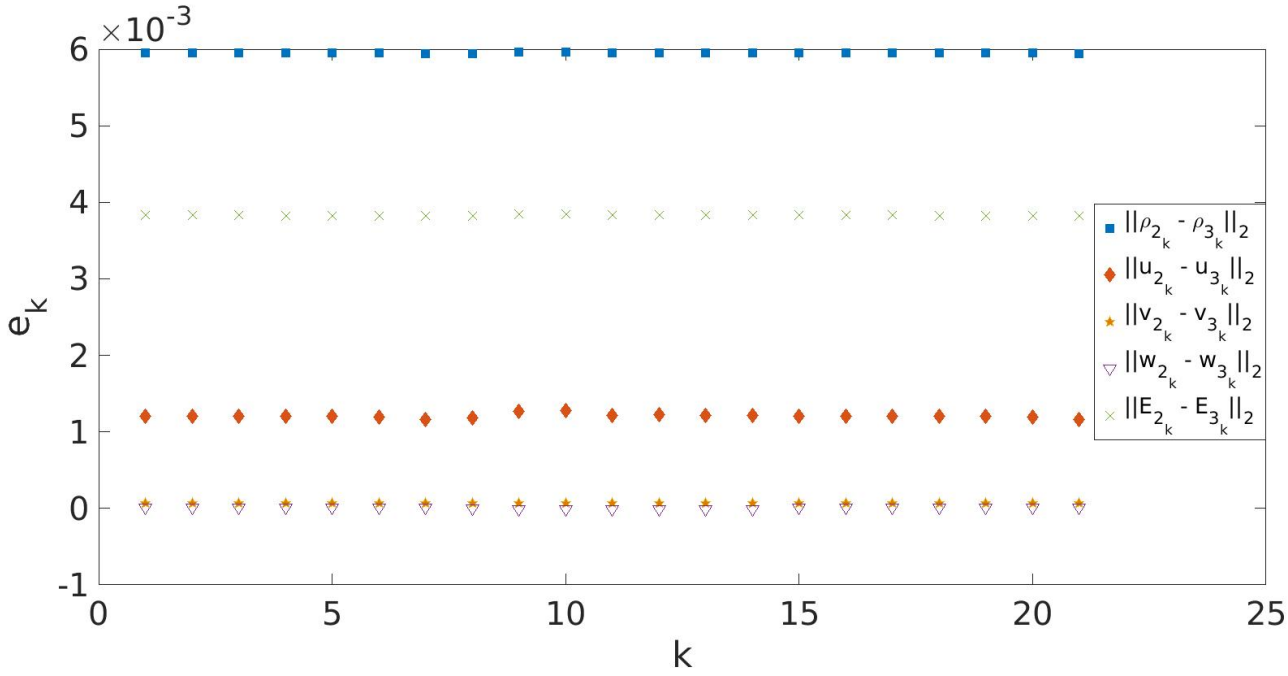

Figure 4.11: The comparison between grids with 41 and 61 points for test with (4.16 – 4.21)

u is deformed and its values are bigger than in the previous case Fig. 4.4b. The velocity v in the plane xy increased as well, Fig. 4.12b and the velocity w is developing a small velocity profile.

The Fig. 4.12d and 4.12f shows the influence of the discontinuity to the u and w velocities from the different angle of view. In the Fig. 4.12e are shown structures of the v velocity, whose values are almost zero in the middle of the channel due to symmetry.

The proper functioning the of periodic boundary conditions is visualized in the Fig. 4.12g and 4.12h. The last Fig. 4.12i displays how the discontinuity is introduced and goes through the whole domain in the w velocity.

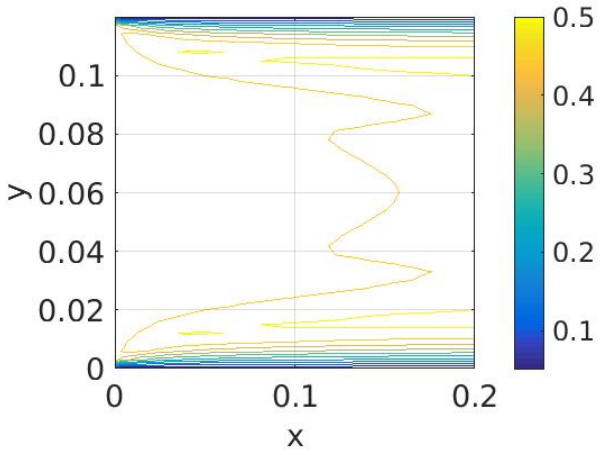

(a) u for 41 grid points test in xy plane, z = 0.06

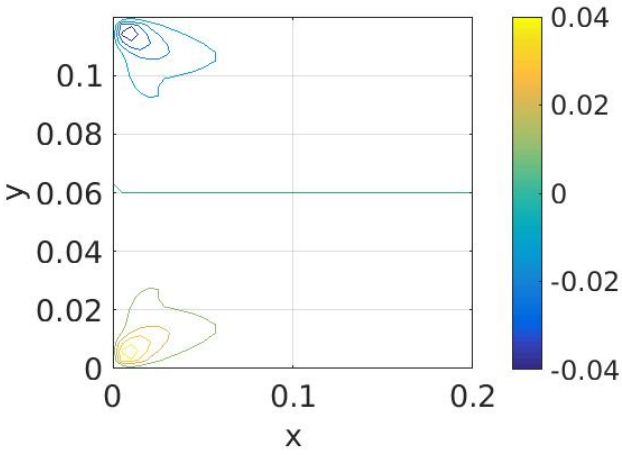

(b) v for 41 grid points test in xy plane , z = 0.06

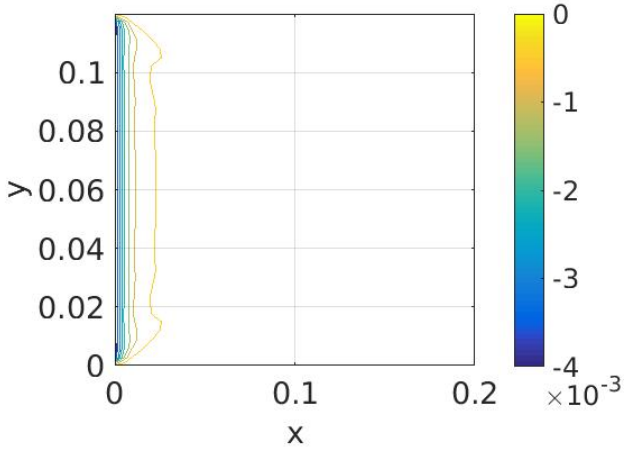

(c) w for 41 grid points test in xy plane , z = 0.06

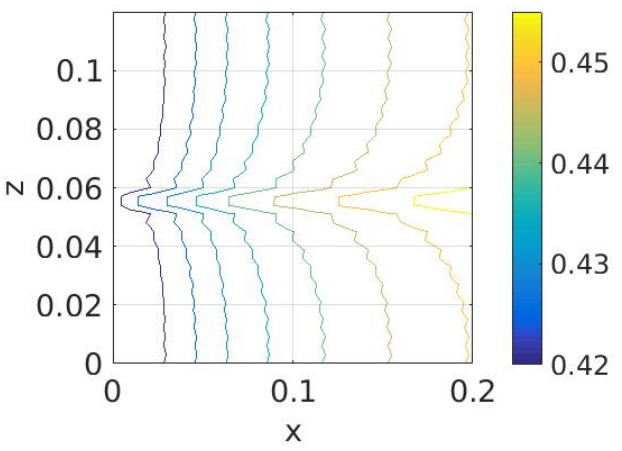

(d) u for 41 grid points test in xz plane, y = 0.06

4.4 3D test case

The last test is chosen with the following parameters. The inlet velocity vector is $\mathbf{u}_0 = (M_{in}, 0, 0.1 \cdot M_{in})$, where $M_{in} = 0.02$ and $Re_{in} = 1000$. The grid is equidistant with 41 points in each direction. $\Delta t = 10^{-3}$ and simulation time $t = 100\ s$, which is the time when graphs are made. Initial pressure and density are

$$\rho_0' = 0, \tag{4.23}$$

$$p_0' = 0. \tag{4.24}$$

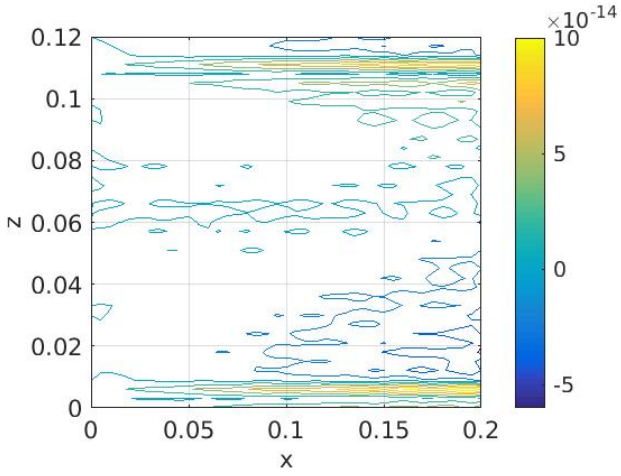

(e) v for 41 grid points test in xz plane, y = 0.06

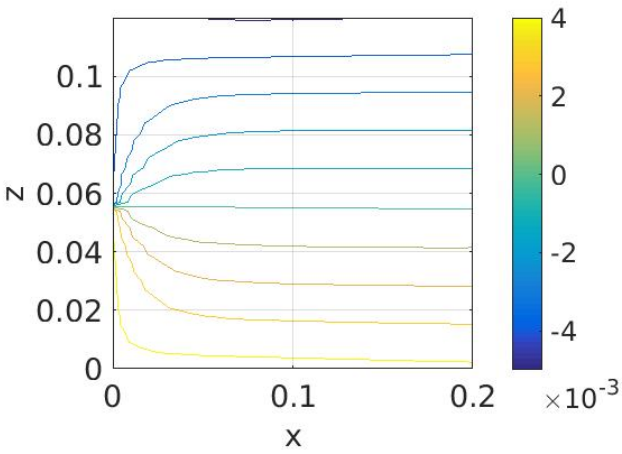

(f) w for 41 grid points test in xz plane, y = 0.06

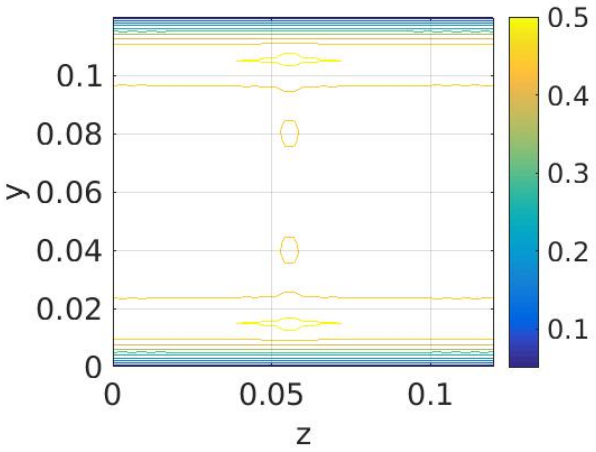

(g) u for 41 grid points test in yz plane, x = 0.1

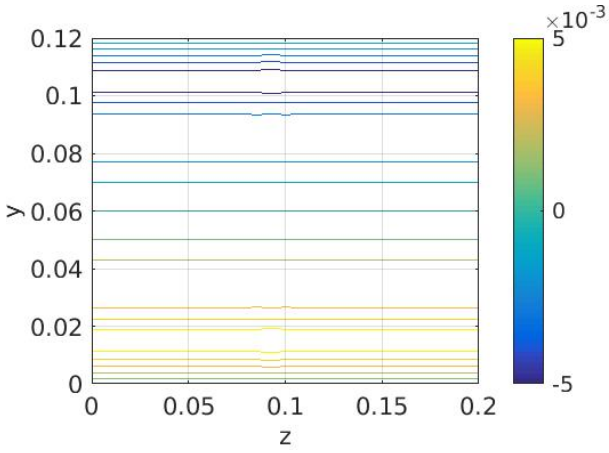

(h) v for 41 grid points test in yz plane, x = 0.1

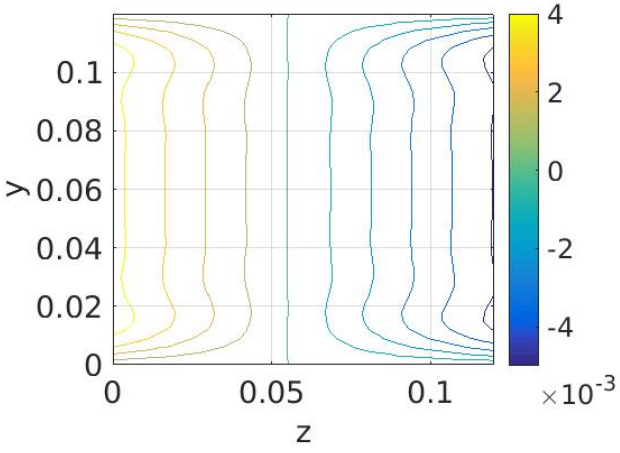

(i) w for 41 grid points test in yz plane, x = 0.1

Figure 4.12: Contours of velocity components in xy, xz and yz planes for 41 grid points test

Since periodic boundary conditions are introduced in the z-direction, all xy planes for $k \in \{1, \ldots, k_{max}\}$ are the same. $k = \frac{k_{max}+1}{2}$ was chosen for visualization in the xy plane.

The profile is developing for u and w velocities component in the xy plane according to Fig. 4.13a and Fig. 4.13c. Since the w velocity at the inlet is ten times smaller than the u velocity, the flow developed less at the end time of simulation. The v velocity in the plane xy has positive and negative values near the walls, this is shown in Fig. 4.13b. The velocity components are shown also in planes xz (Fig. 4.13d, 4.13e, 4.13f). The profile is not developed as in the xy plane because the periodic boundary conditions are introduced there. Results in the plane yz are visualized in Fig. 4.13g, 4.13h, 4.13i. In the yz planes the velocity components are seen to be zero at the walls in the y-direction. Once more the w velocity is ten times smaller than the u velocity. These planes (xz, yz) are always taken with the value $i = \frac{i_{max}+1}{2}$ for the x-direction and $j = \frac{j_{max}+1}{2}$ for the y-direction.

The results are plotted in Matlab.

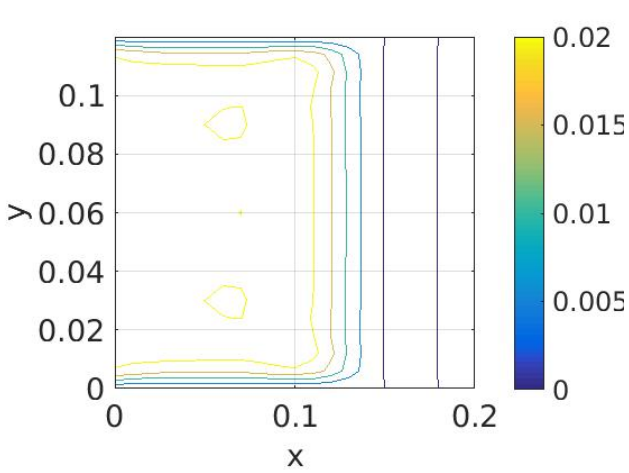

(a) u for 3D test in xy plane, z = 0.06

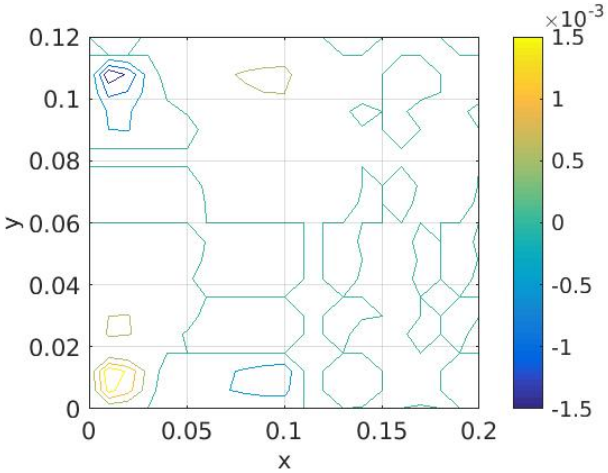

(b) v for 3D test in xy plane, z = 0.06

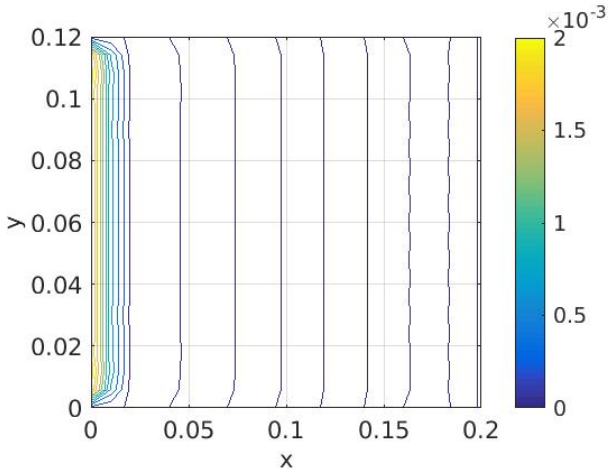

(c) w for 3D test in xy plane, z = 0.06

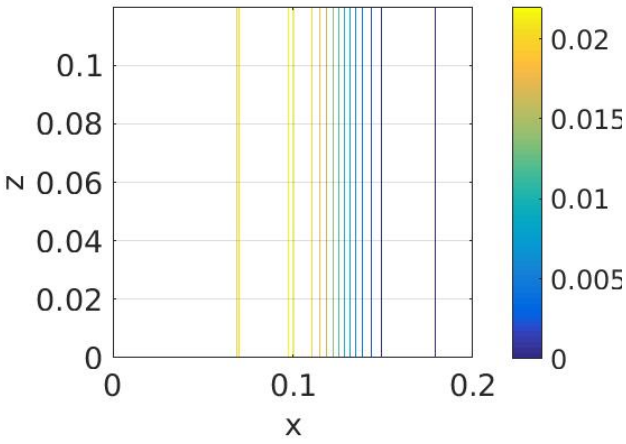

(d) u for 3D test in xz plane, y = 0.06

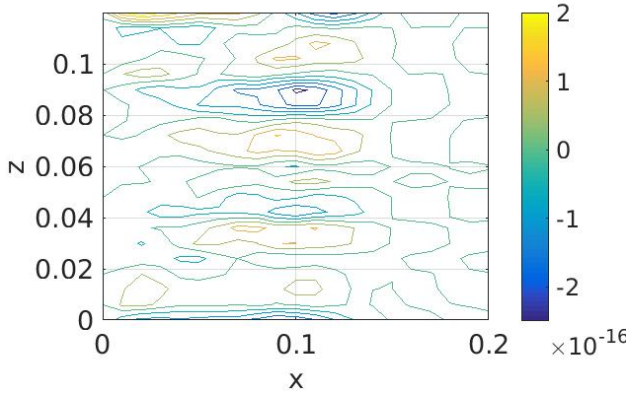

(e) v for 3D test in xz plane, y = 0.06

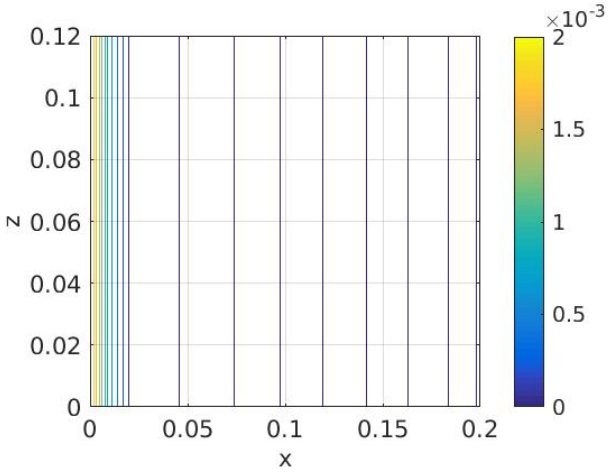

(f) w for 3D test in xz plane, y = 0.06

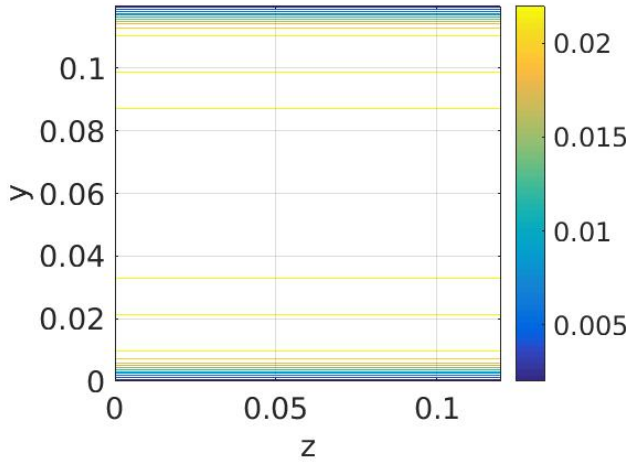

(g) u for 3D test in yz plane, x = 0.1

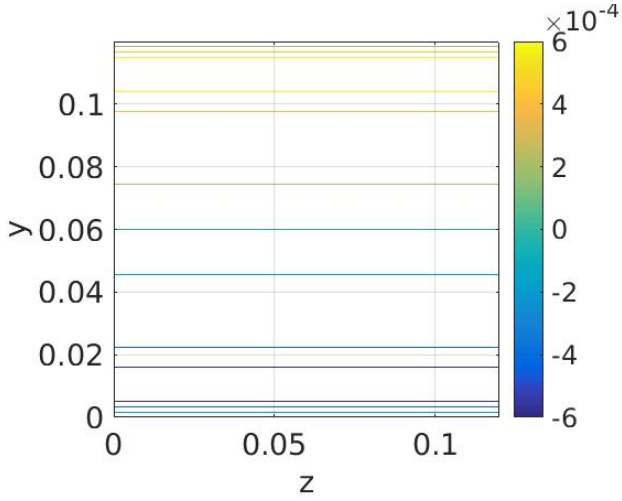

(h) v for 3D test in yz plane, x = 0.1

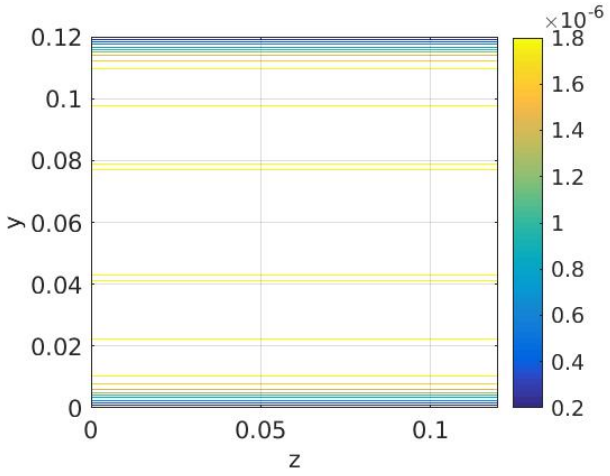

(i) w for 3D test in yz plane, x = 0.1

Figure 4.13: Contours of velocity components in xy, xz and yz planes for 3D channel flow test

Chapter 5

Conclusions and outlook

The main goal of this master thesis was to extend an existing 2D compressible Navier-Stokes code into the third dimension and to get the physical understanding of compressible flow and its numerical solution. The goal was accomplished. The most challenging part of the code conversion into the third dimension was to implement non-reflecting boundary conditions. The discretization of the conservative form of the metric terms for the 3D coordinate transformation also required a lot of work. Periodic boundary conditions were added as part of my job. The most time-consuming part was to debug the code to make it work properly.

The code was tested for several tests cases (uniform flow, 2D case extended into the third dimension, and 3D channel flow) and the results were reported in chapter 4. The grid refinement study showed how the solution depends on the number of grid points for structured grids.

The 3D code works for low Mach and Reynolds number with no complication. The challenge for further work will be to compare the results of this code with a physical experiment in 3D and to implement high order filter for the ζ-direction,

which is currently not used in this code.

Bibliography

[1] EliteRest, "Obstructive sleep apnea," 2017. Available at http://www.eliterest.com/obstructive-sleep-apnea/, date of acces: 2017-04-19.

[2] B. Strand, "Summation by parts for finite difference approximations for d/dx," *Journal of Computational Physics*, vol. 110, no. 1, pp. 47 – 67, 1994.

[3] M. Ho and S. Brass, "Obstructive sleep apnea," *Neurology International*, vol. 3, no. 3, 2011.

[4] J. C. S. Med., "Clinical guideline for the evaluation, management and long-term care of obstructive sleep apnea in adults," *Journal of Clinical Sleep Medicine*, vol. 5, no. 3, pp. 263–276, 2009.

[5] M. Quadrio, C. Pipolo, S. Corti, R. Lenzi, F. Messina, C. Pesci, and G. Felisati, "Review of computational fluid dynamics in the assessment of nasal air flow and analysis of its limitations," *European Archives of Oto-Rhino-Laryngology*, vol. 271, no. 9, pp. 2349–2354, 2014.

[6] I. Weinhold and G. Mlynski, "Numerical simulation of airflow in the human nose," *European Archives of Oto-Rhino-Laryngology and Head & Neck*, vol. 261, no. 8, pp. 452–455, 2004.

[7] Y. Na, K. S. Chung, S.-K. Chung, and S. K. Kim, "Effects of single-sided inferior turbinectomy on nasal function and airflow characteristics.," *Respiratory physiology & neurobiology*, vol. 180 2-3, pp. 289–97, 2012.

[8] M. Hörschler and W. Schröder, "On the assumption of steadyness of nasal cavity flow," *Journal of Biomechanics*, vol. 261, no. 6, pp. 1081–1085.

[9] M. Svärd and J. Nördstrom, "A stable high-order finite difference scheme for the compressible Navier–Stokes equations: No-slip wall boundary conditions," *Journal of Computational Physics*, vol. 227, pp. 4805–4824, 2007.

[10] Svard, M and Carpenter, M. and Nordstrom, J., "A stable high-order finite difference scheme for the compressible Navier–Stokes equations, far-field boundary conditions," *Journal of Computational Physics*, vol. 225, pp. 1020–1038, 2007.

[11] Z. J. Wang, "High-order methods for the Euler and Navier–Stokes equations on unstructured grids," *Progress in Aerospace Sciences*, vol. 43, pp. 1–41, 2007.

[12] Z. Wang, K. Fidkowski, R. Abgrall, F. Bassi, D. Caraeni, A. Cary, H. Deconinck, R. Hartmann, K. Hillewaert, H. Huynh, N. Kroll, G. May, P.-O. Persson, B. van Leer, and M. Visbal, "High-order cfd methods: current status and perspective," *International Journal for Numerical Methods in Fluids*, vol. 72, no. 8, pp. 811–845, 2013.

[13] B. Müller, S. Nordgård, B. Skallerud, and S. G. Johnsen, "Modeling of ob-

structive sleep apnea by fluid-structure interaction in the upper airways," 2014. Available at http://osas.no/.

[14] M. Khalili, M. Larsson, and B. Müller, "Interaction between a simplified soft palate and compressible viscous flow," *Journal of Fluids and Structures*, vol. 67, pp. 85–105, 2016.

[15] M. R. Visbal and D. V. Gaitonde, "On the use of higher-order finite-difference schemes on curvilinear and deforming meshes," *Journal of Computational Physics*, vol. 181, no. 1, pp. 155–185, 2002.

[16] B. Müller, "Linear stability condition for explicit Runge–Kutta methods to solve the compressible Navier-Stokes equations," *Mathematical Methods in the Applied Sciences*, vol. 12, no. 2, pp. 139–151, 1990.

[17] T. Poinsot and S. Lele, "Boundary conditions for direct simulations of compressible viscous flows," *Journal of Computational Physics*, vol. 101, no. 1, pp. 104 – 129, 1992.

[18] K. W. Thompson, "Time dependent boundary conditions for hyperbolic systems," *Journal of Computational Physics*, vol. 68, no. 1, pp. 1 – 24, 1987.

[19] NTNU, "NTNU Vilje cluster," 2017. Available at https://www.hpc.ntnu.no/display/hpc/Vilje.

[20] NOTUR, "UNINETT Sigma2 AS," 2017. Available at http://www.sigma2.no.

Appendix A

High-performance computational cluster Vilje

This chapter is based on [19]. The present research was supported in part by computational resources at NTNU provided by NOTUR [20]. Vilje is a high-performance computational cluster that belongs to NTNU. Table A.1 gives information about its operating environment [19].

Operating system	SUSE Linux Enterprise Server 11
Scheduler	PBS
Compilers	Intel and GNU C and Fortran
MPI library	SGI MPT

Table A.1: Vilje operating environment

The manufacturer is SGI. The cluster has 19.5 racks (1404 nodes) and 22 464 cores and it has 467 teraflops theoretical peak performance. Node details are introduced in table A.2 below.

Number of nodes	1404
Processors per node	2 eight-core processors per node
Processor speed	2.6 GHz
L3 Cache	20 MB / 8 cores
Memory	2GB per core / 32 Gib per Node
Memory type	DDR3 1600 MHz-SDRAM

Table A.2: Vilje node details

A.1 Code uploading

Login is possible only by the secure shell command ssh. The same authentication and security are used by the command scp for transferring the data. Module files have to be loaded before compilation. In this code case, the module files are gcc/4.9.1 for compiler and mpt/2.13 for SGI MPT module. These modules are loaded by

Listing A.1: Module load before execution of code

```
1 module load gcc/4.9.1
2 module load mpt/2.13
```

These commands are part of a bash file named job.sh. The file is listed below.

Listing A.2: job.sh file

```
1 #!/bin/sh
2
3 #PBS -N ns_2d_v_fsi_2
4 #PBS -A ntnu260
5 #PBS -l walltime=100:00:00
6 #PBS -l select=1:ncpus=32:mpiprocs=6
7
```

```
8  module load gcc/4.9.1
9  module load mpt/2.13
10
11 cd $PBS_O_WORKDIR
12
13 mpirun -n 6 ./ns_2d_v_fsi
```

The first line says that this file is a bash file. The set of commands is meant for Vilje. It is a specification of the number of processors, time requested and the name of user's code. cd command is a command for switching between directories and the last command runs the code in parallel.

The last command needed for submitting the job to the pbs queue

Listing A.3: Command for running the code

```
1 qsub job.sh
```

This command sets the program into a queue and returns a notification of the number of your job. The job identifier is used to name the output from the job together. When the job is done, output files are created in the user's file.